

1 **An increase in reactive oxygen species underlies neonatal cerebellum repair**

2
3 Anna Pakula^{1,#}, Salsabiel El Nagar^{1,#}, N. Sumru Bayin^{1,2,3,#}, Jens Bager Christensen^{2,3}, Daniel N.
4 Stephen¹, Adam James Reid², Richard Koche⁴, Alexandra L. Joyner^{1,5,*}

5
6 ¹Developmental Biology Program, Sloan Kettering Institute, New York, NY, USA

7 ²Gurdon Institute, Cambridge University, Cambridge, UK

8 ³Department of Physiology, Development and Neuroscience, Cambridge University, Cambridge,
9 UK

10 ⁴Center for Epigenetics Research, Memorial Sloan Kettering Cancer Center, New York, NY

11 ⁵Biochemistry, Cell and Molecular Biology Program and Neuroscience Program, Weill Cornell
12 Graduate School of Medical Sciences, New York, NY, USA

13 #These authors contributed equally to the work and share first authorship

14 * **Correspondence:**
15 joynera@mskcc.org

16 Keywords: Nestin-expressing progenitors, NEPs, granule cell progenitors, ROS, regeneration

17

18 **Abstract**

19 The neonatal mouse cerebellum shows remarkable regenerative potential upon injury at birth,
20 wherein a subset of Nestin-expressing progenitors (NEPs) undergoes adaptive reprogramming
21 to replenish granule cell progenitors that die. Here, we investigate how the microenvironment of
22 the injured cerebellum changes upon injury and contributes to the regenerative potential of
23 normally gliogenic-NEPs and their adaptive reprogramming. Single cell transcriptomic and bulk
24 chromatin accessibility analyses of the NEPs from injured neonatal cerebella compared to
25 controls show a temporary increase in cellular processes involved in responding to reactive
26 oxygen species (ROS), a known damage-associated molecular pattern. Analysis of ROS levels
27 in cerebellar tissue confirm a transient increased one day after injury at postnatal day 1,
28 overlapping with the peak cell death in the cerebellum. In a transgenic mouse line that ubiquitously
29 overexpresses human mitochondrial catalase (mCAT), ROS is reduced 1 day after injury to the
30 granule cell progenitors, and we demonstrate that several steps in the regenerative process of
31 NEPs are curtailed leading to reduced cerebellar growth. We also provide preliminary evidence
32 that microglia are involved in one step of adaptive reprogramming by regulating NEP
33 replenishment of the granule cell precursors. Collectively, our results highlight that changes in the
34 tissue microenvironment regulate multiple steps in adaptive reprogramming of NEPs upon
35 death of cerebellar granule cell progenitors at birth, highlighting the instructive roles of
36 microenvironmental signals during regeneration of the neonatal brain.

37

38

39

40

41

42

43

44

45

46

47

48 **Introduction**

49

50 The microenvironment surrounding a brain injury and the cellular responses elicited in the
51 remaining cells are key determinants of how efficiently a repair process will unfold. An important
52 factor underlying the effectiveness of regenerative responses to an injury is the plasticity of the
53 stem/progenitor cells in a tissue (Burda and Sofroniew, 2014). The degree to which the
54 microenvironment and specific cell types within it provide pro- or anti-regenerative factors is highly
55 context dependent. The neonatal mouse cerebellum has a remarkable capacity to regenerate
56 cells ablated around birth (Wojcinski et al., 2017, Bayin N. S., 2021, Bayin et al., 2018, Altman
57 and Anderson, 1971). Thus, the cerebellum provides an ideal system to study the roles that
58 signals in the microenvironment play in key steps of the repair process in the brain.

59

60 The cerebellum is a folded hindbrain structure that is critical for motor coordination. It also
61 participates in higher order social and cognitive behaviors through its circuit connections with all
62 other brain regions (Badura et al., 2018, Buckner, 2013, Burda and Sofroniew, 2014, Salman and
63 Tsai, 2016, Strick et al., 2009, Tomlinson et al., 2013). Compared to the rest of the brain, the
64 cerebellum has protracted development, as its major growth occurs during the first two weeks
65 after birth in mice and at least six months surrounding birth in humans (Altman and Bayer, 1997,
66 Rakic and Sidman, 1970, Dobbing and Sands, 1973). This timing of the major growth of the
67 cerebellum makes it susceptible to injury around birth. Indeed, cerebellar hypoplasia is the second
68 leading risk factor for autism spectrum disorders and cerebellar injury around birth can have
69 devastating outcomes and significant effects on subsequent quality of life (Tsai et al., 2018,
70 Stoodley et al., 2017, Wang et al., 2014). Therefore, it is critical to better understand the
71 regenerative processes that allow repair of the cerebellum.

72

73 All the cell types in the cerebellum are derived from two progenitor zones, the embryonic rhombic
74 lip and the ventricular zone that give rise to the excitatory neurons, or the inhibitory neurons and
75 glia, respectively (Leto et al., 2015, Joyner and Bayin, 2022). During postnatal growth, the rhombic
76 lip-derived granule cell precursors (GCPs) cover the surface of the cerebellum in a structure
77 named the external granule layer (EGL) and continue to proliferate in a sonic hedgehog (SHH)
78 dependent manner for two weeks after birth in mice (Wechsler-Reya and Scott, 1999, McMahon
79 et al., 2003, Corrales et al., 2006). Following their exit from the cell cycle, the granule cells (GC)
80 migrate inwards to form the internal granule layer (IGL). Other SHH-dependent progenitor
81 populations of the neonatal cerebellum are either gliogenic Nestin-Expressing Progenitors (NEPs)

82 that express SOX2 and generate astroglia (astrocytes and Bergman glia) or neurogenic-NEPs
83 that generate late born interneurons (Bayin N. S., 2021, Cerrato et al., 2018, Parmigiani et al.,
84 2015). Gliogenic-NEPs reside either in the Bergmann glia layer (BgL) intermixed with Purkinje
85 cells and generate Bergmann glia (Bg) and astrocytes, or in the white matter in the center of the
86 lobules (folds) and generate astrocytes. Neurogenic-NEPs are restricted to the white matter and
87 produce interneurons that migrate outwards to the outermost molecular layer (Bayin N. S., 2021,
88 Brown et al., 2020, De Luca et al., 2015). Surprisingly, when the GCPs are killed upon injury soon
89 after birth, the gliogenic-NEPs in the BgL (BgL-NEPs) undergo adaptive reprogramming to
90 generate GCPs and replenish the EGL via a transitory cellular state that involves upregulation of
91 the neurogenic gene *Ascl1* to promote a glial-to-neural fate switch (Wojcinski et al., 2017, Bayin
92 N. S., 2021). Adaptive reprogramming involves multiple sequential stages starting with increased
93 proliferation of BgL-NEPs, then a fate switch to neuronal progenitors, migration to the site of injury
94 (EGL) and acquisition of a GCP identity. The full repertoire of injury-induced signals that initiate
95 and govern adaptive reprogramming remains to be discovered.

96
97 In the adult brain, numerous cell types communicate and provide a concerted response to injury,
98 including astrocytes, microglia (macrophages of the brain) and stem cells of the neurogenic
99 niches (Frik et al., 2018). The timelines of the cellular responses of each cell type to injury - cell
100 death, activation of microglia, reactive gliosis, proliferation, scar formation and cellular remodeling
101 - have been delineated for specific adult brain injuries, particularly in the cerebral cortex. For
102 example, upon traumatic brain injury cells release damage-associated molecular patterns
103 (DAMPs), which act as an inflammatory stimulus and activate microglia that can lead to gliosis,
104 eventually causing neurotoxicity and scarring (Donat et al., 2017). However, the cellular
105 composition and microenvironment of the early postnatal brain are very different from the adult.
106 In the neonatal cerebellum, microglia are immature (Li et al., 2019) and are still being generated,
107 and NEPs and GCPs are actively proliferating and producing astroglia and neurons. Therefore,
108 the existing knowledge on how adult brain cells react to injury might not apply to the neonatal
109 cerebellum. For example, in the spinal cord, while neonatal microglia and astrocytes facilitate
110 scarless repair, the same cells in the adult promote scarring upon spinal cord injury in mice (Li et
111 al., 2020). It is thus important to study the microenvironment of the neonatal brain during repair
112 to determine what factors promote or inhibit regeneration.

113
114 Dying cells release many factors, including reactive oxygen species (ROS) that activate signaling
115 cascades in neighboring cells. However, little is known about how these signals regulate brain

116 repair, especially during development. The level of ROS during homeostasis is regulated by
117 metabolic processes, and typically is increased following injury (Niethammer, 2016). Furthermore,
118 ROS can directly react with proteins that regulate proliferation, viability, quiescence or
119 differentiation and metabolism (Bigarella et al., 2014, Tan and Suda, 2018). Thus, ROS are
120 considered key signaling molecules that participate in the crosstalk between progenitor cell fate
121 decisions and metabolic switches in a context- and cell type-dependent manner (Bigarella et al.,
122 2014). One significant mechanism by which ROS signaling is implicated during inflammatory
123 responses following an injury is through the activation of microglia, which in turn can lead to more
124 ROS production (Smith et al., 2022). This process is critical as it can potentially promote repair.
125 However, the role of ROS signaling during adaptive reprogramming of NEPs following neonatal
126 cerebellar injury is not known.

127
128 Here we first delineate the sequential changes in the microenvironment upon injury (focused
129 irradiation) to the mouse hindbrain at postnatal day 1 (P1). We then demonstrate a requirement
130 for a transient increase in ROS levels at ~24 hours (hr) post injury for cerebellar regeneration.
131 Single cell RNA-sequencing (scRNA-seq) and bulk Assay for Transposase-Accessible Chromatin
132 with sequencing (ATAC-seq) analyses revealed increased ROS signaling compared to controls
133 that peaks 24 hr after injury in NEPs, demonstrating that ROS is an acute signal associated with
134 the NEP response to GCP death. A functional role of ROS signaling was established using a
135 transgene (*mCAT*) that expresses the human mitochondrial Catalase which can reduce ROS
136 levels broadly. Several key steps in adaptive reprogramming were abrogated in *mCAT*/⁺ mice
137 leading to reduced replenishment of the EGL and a smaller adult cerebellum. Finally, we show
138 that the density of microglia is reduced at P5 in irradiated *mCAT* mice compared to controls and
139 provide preliminary evidence that microglia play a role in the step of replenishing the EGL with
140 BgL-derived GCPs during adaptive reprogramming.

141

142 **Materials and Methods**

143 **Animals**

144 All the mouse experiments were performed according to protocols approved by the Institutional
145 Animal Care and Use Committee of Memorial Sloan Kettering Cancer Center (MSKCC) (protocol
146 no. 07-01-001). Animals were housed on a 12-hour light/dark cycle and given access to food and
147 water ad libitum.

148

149 Two mouse lines were used in this study: *Nes-Cfp* (JAX #034387) (Encinas et al., 2006) and
150 *mCAT* (JAX #016197) (Schriner et al., 2005). Animals were maintained on an outbred Swiss
151 Webster background. Both sexes were used for analyses except for the genomics experiments
152 (scRNA-seq and ATAC-seq) where males were used.

153

154 *EdU administration*

155 5-ethynyl-2'-deoxyuridine (EdU) stock was dissolved in sterile phosphate-buffered saline (PBS)
156 at 10 mg/mL and a dose of 5 μ g/g was intraperitoneally injected into animals 1 hour prior to
157 euthanasia.

158

159 *PLX5622 administration*

160 PLX5622 powder was provided by Plexxikon under a Materials Transfer Agreement. PLX5622
161 powder was first diluted in DMSO at 20mM and then diluted 1X in PBS just before intraperitoneal
162 injection into newborn pups. Injections were given every day from P1 to P8 at a dose of 10 μ g/g
163 of body weight. Control pups were injected with PBS-DMSO vehicle control.

164

165 *Irradiation*

166 P1 mice were anesthetized by hypothermia and given a single dose of ~5Gy γ -irradiation in an X-
167 RAD 225Cx (Precision X-ray) Microirradiator in the MSKCC Small-Animal Imaging Core facility.
168 A 5-mm diameter collimator was used to target the hindbrain from the left side of the animal.

169

170 **Tissue preparation and histology**

171 For immunocytochemistry, animals younger than P8 were sacrificed and then brains were
172 dissected, fixed in 4% paraformaldehyde for 24 hr at 4°C, cryoprotected in 30% sucrose in
173 phosphate-buffered saline (PBS) until they sank and then frozen in Cryo-OCT (Tissue-Tek). Older
174 animals were anesthetized and then perfused with cold PBS followed by 4% paraformaldehyde
175 prior to brain dissection. Frozen brains were cryosectioned sagittally at 14 μ m and slides stored
176 at -20°C. Midline cerebellar sections were used for quantification in all downstream analyses.

177

178 For immunofluorescence staining, slides were allowed to warm to room temperature (RT) and
179 washed 3 times in PBS. Then, tissues were blocked for one hour with blocking buffer (5% BSA
180 (w/v) in 1XPBS with 0.1% Triton-X) at RT. Primary antibodies diluted in the blocking buffer were
181 placed on slides for overnight incubation at 4°C. Slides were then washed in PBS with 0.1%
182 Triton-X and incubated with fluorophore-conjugated secondary antibodies diluted in the blocking

183 buffer for 1 hr at RT. Following washes in PBS with 0.1% Triton-X after the secondary antibody
184 incubation, nuclei were counterstained with Hoechst (1:3000) and the slides were mounted using
185 mounting media (Electron Microscopy Sciences). Primary antibodies used are described in Table
186 S1 and secondary antibodies were Alexa Fluor-conjugated secondary antibodies (1:1000).

187

188 EdU was detected using a Click-it EdU (Invitrogen, C10340) assay with Sulfo-Cyanine5 azide
189 (Lumiprobe Corporation, A3330).

190

191 For TUNEL staining, after primary antibody incubation and washes, sections were permeabilized
192 in PBS with 0.5% TritonX-100 for 10 minutes (min) and then pre-incubated in TdT buffer (30mM
193 Tris HCl, 140 mM sodium cacodylate and 1mM CoCl₂) for 15 min at RT. Slides were then
194 incubated for 1hr at 37°C in TUNEL reaction solution containing Terminal Transferase and
195 Digoxigenin-11dUTP (Roche). After the TUNEL reaction and washes, slides were incubated with
196 a secondary antibody solution which included a sheep anti-dioxigenin-rhodamine (Roche) for the
197 visualization of TUNEL reaction.

198

199 **Image acquisition and analysis**

200 Images were collected with a DM6000 Leica microscope, a NanoZoomer Digital Pathology
201 microscope (Hamamatsu Photonics), or an LSM880 confocal microscope (Zeiss). Images were
202 processed using NDP.view2 software, ImageJ software (NIH, Bethesda, MA, USA) and
203 Photoshop (Adobe).

204

205 **Cell dissociation for FACS and flow cytometry**

206 Cerebella were dissected into ice-cold 1x Hank's Buffered Salt Solution (Gibco) and dissociated
207 using Accutase (Innovative Cell Technologies) at 37°C for 10-15 min. After dissociation, Accutase
208 was diluted with 3x excess volume of neural stem cell media (Neurobasal medium, supplemented
209 with N2, B27 (without vitamin A)), and nonessential amino acids (Life Technologies, Gibco) and
210 cells were filtered using a 40 µm mesh cell strainer. After 5 min of centrifugation in a chilled
211 centrifuge at 500g, the pellet was resuspended in neural stem cell media and strained using
212 strainer cap tubes (Falcon) for downstream experimentation. All centrifugation was performed at
213 4°C and cells were kept on ice when possible.

214

215 **Flow cytometry analysis for ROS and mitochondria mass**

216 For MitoSOX and MitoTracker analyses, cells were incubated for 30 min at 4°C with 5 μ M of
217 MitoSOX and 100 μ M of MitoTracker (Thermo Fisher Scientific) to assess mitochondrial
218 superoxide production and mitochondrial mass, respectively. Data were collected using a LSR
219 Fortessa flow cytometer (BD) and analyzed using FlowJo software. The gating for the MitoSOX
220 or MitoTracker high populations (top 90%) were performed as previously described (Clutton et
221 al., 2019)

222

223 **Multiplexed sc-RNAseq**

224 *Sample preparation*

225 2-4 *Nes-Cfp/+* cerebella/replicates from male control non-irradiated pups or pups that were
226 irradiated at P1 were collected at P1 (control only), P2, P3 and P5 and dissociated as described
227 above. All conditions were performed in 2 replicates for nonIR and IR conditions, except for P5.
228 Following dissociation, CFP+ cells were immediately sorted on a BD FACS Aria sorter (BD
229 Biosciences) using a 100 μ m nozzle. 50,000 Nes-CFP+ cells from each sample were processed
230 for scRNA-seq. Cells were sorted into neural stem cell media.

231

232 *Multiplexing, droplet preparation, sequencing and data processing*

233 The scRNA-Seq of FACS-sorted Nes-CFP+ cell suspensions was performed on a Chromium
234 instrument (10X genomics) following the user guide manual for 3' v3.1. In brief, 50,000 FACS-
235 sorted cells from each condition were multiplexed using CellPlex reagents (10x Genomics) as
236 described by the manufacturer's protocol. P3 nonIR replicate #2 did not yield sufficient cells after
237 multiplexing. The viability of cells was above 95%, as confirmed with 0.2% (w/v) Trypan Blue
238 staining and barcoded cells were pooled into a single sample in PBS containing 1% bovine serum
239 albumin (BSA) to a final concentration of 700–1,300 cells per μ l. 2-3,000 cells were targeted for
240 each sample. Samples were multiplexed together on one lane of a 10X Chromium following
241 the 10x Genomics 3' CellPlex Multiplexing protocol and a total of ~30,000 cells were targeted for
242 droplet formation. Cells were captured in droplets. After the reverse transcription and cell
243 barcoding in droplets, emulsions were broken, and cDNA was purified using Dynabeads MyOne
244 SILANE followed by PCR amplification per the manufacturer's instruction. Final libraries were
245 sequenced on an Illumina NovaSeq S4 platform (R1 – 28 cycles, i7 – 8 cycles, R2 – 90 cycles)
246 by the MSKCC core facility.

247

248 *Data Analysis*

249 Single-cell RNA-seq fastq files were demultiplexed using sharp (<https://github.com/hisplan/sharp>)
250 and initially mapped to the mouse mm10 reference genome using Cell Ranger v6.0.1 (Zheng et
251 al., 2017). The Cell Ranger BAM files for individual samples were then converted back to fastq
252 files using *bamtofastq* (Cell Ranger v7.0.1), with `--reads-per-fastq=1000000000`. Reads were then
253 mapped to the GRCm39 mouse reference with Gencode annotations (vM30) using STARsolo
254 v2.7.10a (`--soloFeatures Gene Velocity`, `--soloType CB_UMI_Simple`, `--soloCBwhitelist 3M-`
255 `february-2018.txt`, `--soloUMIlen 12`, `--soloCellFilter EmptyDrops_CR`, `--soloMultiMappers EM`)
256 (Kaminow et al., 2021, Frankish et al., 2021).

257
258 The STARsolo output was used to create Seurat (v4.3) objects for each sample with spliced and
259 unspliced read count matrices (Hao et al., 2021). The objects were integrated, by running
260 `NormalizeData` and `FindVariableFeatures` (`selection.method = "vst"`, `nfeatures = 3000`) on each
261 one, then `SelectIntegrationFeatures` and `FindIntegrationAnchors` on the list of objects and finally
262 `IntegrateData` with the anchors. Counts were then normalized with `SCTransform`. Based on
263 manual analysis, cells were filtered out where number of detected genes was $\leq 1,500$, number of
264 detected transcripts was $\geq 40,000$ and mitochondrial gene percentage $\geq 5\%$. To determine cell
265 cycle phases, the Kowalczyk et al. (Kowalczyk et al., 2015) cell cycle markers were used,
266 assuming the gene names, capitalized to the title case, to be orthologous between mouse and
267 human with the `CellCycleScoring` function. `SCTransform` was used to regress out the “Cell Cycle
268 difference” score (`S score – G2M score`). Dimension reduction was performed using `RunPCA` and
269 `RunUMAP` (`dims = 1:20`, `n.neighbors = 30`). For clustering, `FindNeighbors` was run using the first
270 20 principal components, then `FindClusters` with the Leiden algorithm with the default settings
271 (Traag et al., 2019). Clusters were annotated using known markers: GCPs
272 (*Atoh1*+/*Barhl1*+/*Tubb3*+), BgL-NEPs (*Hopx*+), ependymal cells (*Foxj1*+), immature interneurons
273 (*Pax2*+), Neurogenic NEPs (*Ascl1*+), astrocytes (*Slc6a11*+), oligodendrocytes (*Olig1*+),
274 meninges (*Col3a1*+/*Vtn*+/*Dcn*+), microglia (*Ly86*+/*Fcer1g*+).

275
276 The differential gene expression analyses were performed individually on *Hopx*+ gliogenic-NEPs,
277 *Ascl1*+ neurogenic-NEPs, and GCPs following the same computational workflow. First, clusters
278 containing *Hopx*-NEPs (clusters 2, 3, 6, 10), *Ascl1*-NEPs (clusters 5, 8, 11), or GCPs (clusters 1,
279 4, 7, 12, 14) were subsetted from the original data set based on the expression of *Hopx*, *Ascl1*,
280 and *Atoh1*, *Barhl1* and *Rbfox*, respectively. Second, the subsetted cells were divided according
281 to whether the cells were from P2 or P3+P5 and split based on their biological replicate. The split
282 data sets were normalized using `NormalizeData` with default parameters, and the 3,000 top

283 variable features were computed using FindVariableFeatures with default settings. Re-integration
284 of the data sets was subsequently performed using SelectIntegrationFeatures,
285 FindIntegrationAnchors, and IntegrateData all with default parameters as previously described,
286 except for IntegrateData in the *Asc/1+* neurogenic-NEP analyses where $k.weight = 50$ was used.
287 Following re-integration, SCTransform with default parameters was used to normalize
288 mitochondrial read percentage, cell cycle difference score, number of features, and number of
289 counts. Dimension reduction was thereafter performed using RunPCA with default parameters
290 and RunUMAP with default parameters except $dims = 1:40$, $repulsion.strength = 0.1$, and $min.dist$
291 $= 0.5$. Clustering was subsequently performed using FindNeighbors with default settings except
292 $dim = 30$ and FindClusters with default settings for resolutions between 0.1 and 3 using the
293 original Louvain algorithm. A final resolution which gave a high silhouette score with a relatively
294 low negative silhouette proportion was selected for individual data sets. To allow downstream
295 DESeq2 analyses, count matrices were constructed by aggregating counts from cells from the
296 same treatment condition and biological replicate using AggregateExpression. The aggregated
297 count matrices were converted into a DESeq2 dataset object using DESeqDataSetFromMatrix,
298 grouping the samples by treatment conditions. Genes with fewer than 10 counts were filtered out.
299 DESeq2 (v1.36.0) was used to perform the differential expression analyses using a negative
300 binomial distribution and default settings (Love et al., 2014). The results were visualized using
301 EnhancedVolcano with a fold change cut-off of ± 0.5 and an adjusted p-value threshold of 0.05.

302

303 The GO term analyses were performed on differentially expressed genes from the DESeq2 results
304 filtered with a \log_2 fold change threshold of ± 0.5 and an adjusted p-value threshold of 0.05 for
305 each comparison. The probability weight function was computed using nullp with default
306 parameters and the mm8 mouse genome. The background genes used to compute the GO term
307 enrichment includes all genes with gene symbol annotations within mm8. The category
308 enrichment testing was performed using goseq with default parameters from the goseq package
309 (v1.48.0).

310

311 **Bulk ATAC-seq**

312 *Sample preparation*

313 FACS-sorted Nes-CFP+ cells (30,000-50,000 per replicate) were isolated from control or
314 irradiated (at P1) P2 cerebella. 2-3 cerebella were pooled for each sample. Cells were
315 immediately processed for nuclei preparation and transposition using the OMNI-ATAC protocol

316 (Corces et al., 2017). Sequencing was performed at the MSKCC genomics core facility using the
317 Illumina NovaSeq S4 platform.

318

319 *Data Processing and Analysis*

320 Raw sequencing reads were 3' trimmed and filtered for quality and adapter content using version
321 0.4.5 of TrimGalore (https://www.bioinformatics.babraham.ac.uk/projects/trim_galore), with a
322 quality setting of 15, and running version 1.15 of cutadapt and version 0.11.5 of FastQC. Version
323 2.3.4.1 of bowtie2 (<http://bowtie-bio.sourceforge.net/bowtie2/index.shtml>) was used to align reads
324 to mouse assembly mm10 and alignments were deduplicated using MarkDuplicates in version
325 2.16.0 of Picard Tools. Enriched regions were discovered using MACS2
326 (<https://github.com/taoliu/MACS>) with a p-value setting of 0.001, filtered for blacklisted regions
327 ([http://mitra.stanford.edu/kundaje/akundaje/release/blacklists/mm10-](http://mitra.stanford.edu/kundaje/akundaje/release/blacklists/mm10-mouse/mm10.blacklist.bed.gz)
328 [mouse/mm10.blacklist.bed.gz](http://mitra.stanford.edu/kundaje/akundaje/release/blacklists/mm10-mouse/mm10.blacklist.bed.gz)), and a peak atlas was created using +/- 250 bp around peak
329 summits. The BEDTools suite (<http://bedtools.readthedocs.io>) was used to create normalized
330 bigwig files. Version 1.6.1 of featureCounts (<http://subread.sourceforge.net>) was used to build a
331 raw counts matrix and DESeq2 was used to calculate differential enrichment for all pairwise
332 contrasts. Peak-gene associations were created by assigning all intragenic peaks to that gene,
333 while intergenic peaks were assigned using linear genomic distance to transcription start site.
334 Network analysis was performed using the assigned genes to differential peaks by running
335 `enrichplot::cnetplot` in R with default parameters. Composite and tornado plots were created using
336 `deepTools v3.3.0` by running `computeMatrix` and `plotHeatmap` on normalized bigwigs with
337 average signal sampled in 25 bp windows and flanking region defined by the surrounding 2 kb.
338 Motif signatures were obtained using Homer v4.5 (<http://homer.ucsd.edu>) on differentially
339 enriched peak *regions*.

340

341 **Data and code availability**

342 The scRNA-seq data was submitted to ArrayExpress (Accession E-MTAB-13353). Bulk ATAC-
343 seq data has been submitted to GEO (GSE269342). The code used to carry out the scRNA-seq
344 analysis can be found on GitHub repository: https://github.com/BayinLab/Pakula_et_al_23

345

346 **Quantification and statistical analysis**

347 For detecting TUNEL, IBA1, GFAP, CFP and SOX2, images were captured using a DM600 Leica
348 fluorescent microscope and subsequently quantified on ImageJ Software (NIH). Measurements
349 were conducted on lobules 3, 4 and 5 of midsagittal sections unless indicated in Figure legends.

350 Positive cells were counted and densities were calculated based on BgL length, EGL area, WM
351 area or on the whole cerebellum without the EGL (outside EGL) as indicated in the figures. For
352 the cerebellar section area, images were acquired using a Nanozoomer2.0 HT slide scanner
353 (Hamamatsu). Midsagittal sections were selected and exported for manual analysis using ImageJ
354 software. For EGL thickness, images of lobules 3, 4 and 5 from midsagittal sections were obtained
355 using a DM600 Leica fluorescent microscope and analyzed on ImageJ. EGL thickness was
356 calculated as the EGL area divided by the EGL perimeter.

357
358 Prism (GraphPad) was used for all statistical analyses. Statistical tests performed in this study
359 were Welch's two-tailed t-test and Two-way analysis of variance (ANOVA) followed by post hoc
360 analysis with Tukey's multiple comparison tests. A p-value ≤ 0.05 was considered as significant.
361 Results are presented as the mean \pm SEM. At least three biological samples and 2 to 3 sections
362 per sample were analyzed for each experiment to ensure reproducibility and the sample sizes are
363 reported in the Results section for significant data. For qualitative analysis, midsagittal sections
364 from at least 4 samples were observed.

365 366 **Results**

367 368 **scRNA-seq of NEPs during adaptive reprogramming reveals increased cellular stress, ROS** 369 **signaling and DNA damage**

370
371 To investigate the molecular changes that NEP subpopulations undergo upon injury to the EGL,
372 in particular an increase in the signaling pathways associated with injury induced cellular stress
373 and ROS, we performed multiplexed scRNA-seq of CFP+ cells isolated by fluorescence-activated
374 cell sorting (FACS) of cerebella from *Nes-Cfp*+ transgenic neonates either irradiated at P1 (IR;
375 P2, P3, P5) or non-irradiated (nonIR; P1, P2, P3, P5) (Figure 1A, Supplementary Figure 1A, B).
376 Following the filtering out of poor quality cells and integration of replicates and the two conditions,
377 the clustering of 11,878 cells (6,978 nonIR and 4,900 IR) was performed (Hao et al., 2021). The
378 analysis revealed the expected three distinct groups of cells: gliogenic-NEPs and astrocytes
379 (*Hopx*+ clusters 2, 3, 6, 10), neurogenic-NEPs (*Ascl1*+ clusters 5, 8, 11) and GCP (*Atoh1*+
380 clusters 1, 4, 7, 12, 14) that were present at each stage and in both conditions (Figure 1B-E,
381 Supplementary Figure 1C-F, Table S2). These groups of cells were further subdivided into
382 molecularly distinct clusters based on marker genes and their cell cycle profiles or developmental
383 stages (Figure 1D, Table S2). In addition, oligodendrocyte progenitors (cluster 15), microglia
384 (clusters 17, 21), ependymal cells (clusters 13, 18, 19) and meninges (cluster 16) were detected

385 (Figure 1B, D, Table S2). Cluster 20 represented low-quality cells and was omitted from
386 downstream analyses. As expected, the GCP clusters were enriched in the cells from irradiated
387 mice and at P5 (Supplementary Figure 1C). Detection of *Nes* mRNA confirmed that the transgene
388 reflects endogenous *Nes* expression in progenitors of many lineages, and also that the
389 perdurance of CFP protein in immediate progeny of *Nes*-expressing cells allowed the isolation of
390 these cells by FACS (Figure 1E).

391
392 Our further analyses focused on changes in the signaling pathways associated with injury induced
393 cellular stress and ROS. We previously showed that a subset of the *Hopx*⁺ gliogenic-NEPs that
394 are present in the BgL are the ones that undergo adaptive reprogramming following GCP death
395 (Wojcinski et al., 2017, Bayin N. S., 2021). We therefore assessed the immediate and later effects
396 of GCP death on *Hopx*⁺ gliogenic-NEPs by performing differential expression analyses between
397 nonIR and IR gliogenic-NEPs (*Hopx*⁺, clusters 2, 3, 6, 10) at P2, or at P3 and P5 (P3+5). 24 hr
398 after injury at P1, 132 genes in gliogenic-NEP clusters were significantly upregulated in IR
399 compared to 34 genes that were upregulated in nonIR P2 cells (adjusted p-value \leq 0.05, Figure
400 1F, Table S3). The significantly increased genes included *Cdkn1a*, *Phlda3*, *Ass1* and *Bax*, all of
401 which have been implicated as increased in response to DNA damage and in ROS signaling, as
402 well as in anti-apoptotic functions (Figure 1G) (Masgras et al., 2012, Bensellam et al., 2019, Qiu
403 et al., 2014, Jiang et al., 2008). Indeed, many of the significant gene ontology (GO) terms
404 associated with the genes upregulated in gliogenic-NEPs with injury were related to response to
405 irradiation, DNA damage, the P53 pathway and ROS metabolic processes, whereas many of the
406 significant GO terms associated with the genes upregulated in the nonIR cells at P2 were related
407 to metabolic processes (p-value \leq 0.05, Figure 1H, Table S4). Interestingly, the transcriptional
408 changes observed at P2 were less pronounced at later time points, where although some of the
409 top differentially expressed genes at P2 were still significantly upregulated at P3+5 stages
410 combined (e.g. *Cdkn1a*, *Phlda3*, *Ass1*, *Bax*), the increase in expression levels of these genes
411 upon injury and/or the number of cells expressing them gradually declined after P2 in IR gliogenic-
412 NEPs when compared to their nonIR counterparts (Figure 1G). Genes upregulated in IR P3+5
413 gliogenic NEPs were associated with similar GO terms to those at P2, such as response to
414 irradiation and the P53 pathway, however, “ROS metabolic processes” was no longer a
415 significantly enriched GO term (p-value \leq 0.05, Supplementary Figure 2A, F, Table S3-4).

416
417 To further assess the injury induced transcriptional signatures, we performed the same differential
418 expression analysis on nonIR and IR neurogenic-NEPs (*Ascl1*⁺, clusters 5, 8, 11) and GCPs

419 (*Atoh1*⁺, clusters 1,4,7,12,14) at P2, or at P3+P5 to identify the immediate and later changes
420 upon injury at birth. Some of the DNA damage and apoptosis related genes that were upregulated
421 in IR gliogenic-NEPs (*Cdkn1a*, *Phlda3*, *Bax*) were also upregulated in the IR neurogenic-NEPs
422 and GCPs at P2 (Supplementary Figure 2B-E). Similar to the gliogenic-NEPs, P2 IR neurogenic-
423 NEPs showed significant upregulation of genes associated with GO terms related to stress
424 response and apoptosis following injury, although the ROS related GO term was not as prominent
425 (Supplementary Figure 2B, G, Table S3-4). Interestingly, although IR neurogenic-NEPs at P3+5
426 had only 27 genes that were significantly upregulated following injury (adjusted p-value \leq 0.05,
427 Table S3, Supplementary Figure 2C), the genes included ones associated with neural stem cells
428 and BgL-NEPs (e.g. *Id1*, *Apoe*, *Ednrb*). The latter genes could represent the transitory *Ascl1*⁺
429 BgL-NEP population that induces *Ascl1* expression during adaptive reprogramming and would be
430 included in the *Ascl1*⁺ neurogenic clusters or reflect the delayed neurogenesis of neurogenic-
431 NEPs previously demonstrated (Bayin N. S., 2021). Consistent with the latter, the nonIR P3+5
432 neurogenic-NEPs showed an increase in mature neuron markers compared to IR cells (adjusted
433 p-value $<$ 0.05, Supplementary Figure 2C, H, Tables S3-4).

434
435 In contrast to the gliogenic- and neurogenic-NEP subtypes, P2 IR GCPs showed upregulation of
436 genes enriched in GO terms such as neural differentiation and axonogenesis as well as ROS
437 signaling and nonIR P2 GCPs showed increased expression of genes involved in cell cycle and
438 mitosis (Supplementary Figure 2D, I). This result could reflect the death of highly proliferative
439 GCPs after irradiation and sparing of only postmitotic granule cells upon irradiation at P1. P3+5
440 IR GCPs showed increased expression of genes associated with BgL-NEPs (*Id1* and *Gdf10*,
441 adjusted p-value \leq 0.05) and genes associated with GO terms such as cell cycle and cell fate
442 commitment whereas P3+5 nonIR GCPs showed enrichment for GO terms related to cell
443 migration and neurogenesis (adjusted p-value \leq 0.05, Supplementary Figure 2D, E, I, J, Tables
444 S3-4). This result could reflect the delayed neurogenesis of GCPs following injury. Interestingly,
445 we did not observe significant enrichment for GO terms associated with cellular stress response
446 in the GCPs that survived the irradiation compared to controls, despite significant enrichment for
447 ROS signaling related GO-terms (Table S4). Collectively, these results indicate that injury induces
448 significant and overlapping transcriptional changes in NEPs and GCPs. The gliogenic- and
449 neurogenic-NEP subtypes transiently upregulate stress response genes upon GCP death, and
450 an overall increase in ROS signaling is observed in the injured cerebella.

451

452 **Injury induces changes in NEP chromatin landscape at P2**

453

454 We next tested whether GCP death at birth induces changes to the chromatin landscape of NEPs
455 that reflect the altered gene expression observed with scRNA-seq, by performing bulk ATAC-seq
456 on FACS-isolated CFP+ cells from P2 control and injured *Nes-Cfp/+* pup cerebella (Figure 1A).
457 P2 was chosen as it is the stage when GCPs contribute the least to the total Nes-CFP+ FACS
458 population and to identify the immediate effects of the injury on NEP chromatin. Analysis of
459 differentially open chromatin showed that injury induces major changes to the chromatin
460 landscape of the NEPs (1168 differentially open regions, adjusted p-value<0.05, Figure 1I. Table
461 S5). Of interest, *Cdkn1a* and *Phlda3*, two genes stimulated by ROS and injury (Bensellam et al.,
462 2019, Masgras et al., 2012) and that were upregulated in gliogenic-NEPs after irradiation (Figure
463 1F-G, Supplementary Figure 2B) exhibited new accessible regions around their gene bodies
464 compared to the nonIR P2 Nes-CFP+ cells (Figure 1J). However, not all genes in the accessible
465 areas were differentially expressed in the scRNA-seq data. While some of this could be due to
466 the detection limits of scRNA-seq, further analysis is required to assess the mechanisms of how
467 the differentially accessible chromatin affects transcription. Known motif analysis in the regions
468 with increased accessibility upon injury showed enrichment for binding motifs of the JUN/AP1
469 transcriptional complex (p-value = 10^{-14} , % of target sequences with motif = 15%, Table S6) which
470 is known to act in response to cellular stress and be activated by ROS. In addition, the DNA
471 binding site for FOXO3, a transcription factor that regulates ROS levels, had increased chromatin
472 accessibility (p-value = 0.001, % of target sequences with motif = 22.41%) (Table S6) (Filosto et
473 al., 2003, Auten and Davis, 2009, Hagenbuchner et al., 2012). Finally, linkages between the
474 genes in differentially open regions identified by ATAC-seq and the associated GO-terms
475 revealed an active transcriptional network involved in regulating cell death and apoptosis (Figure
476 1K). Furthermore, some of the genes involved in this response, such as *Ppara*, *Egln3*, *Foxo3*, *Jun*
477 and *Nos1ap*, have been implicated as upregulated with increased ROS levels or involved in ROS
478 signaling (Devchand et al., 2004, Kaelin, 2005, Hagenbuchner et al., 2012, Filosto et al., 2003).
479 In summary, our ATAC-seq data analysis along with the scRNA-seq provide strong evidence that
480 irradiation causes increased ROS signaling in the BgL-NEPs upon GCP death by inducing
481 transcriptional and epigenetic changes within 1 day after injury (P2). In addition, genes related to
482 cell survival and death, cellular stress and DNA damage are upregulated in NEPs shortly upon
483 injury, possibly as a means to overcome the cellular effects of injury and induce adaptive
484 reprogramming of NEPs to replenish the lost cells.

485

486 **Transient increase in cerebellar ROS during apoptosis of granule cell precursors**

487

488 To validate that the transient increase in expression of genes associated with cellular stress and
489 ROS signaling is due to an increase in ROS upon cerebellar injury, we quantified ROS levels in
490 whole cerebellum samples using a mitochondrial superoxide indicator (MitoSOX) via flow
491 cytometry. A significant increase in ROS (cells present in the top 90% MitoSOX+ intensity) was
492 observed specifically at P2 ($p=0.0005$, $n\geq 10$) and not at P3 or P5 in IR pups compared to nonIR
493 (Figure 2A, B and Supplementary Figure 3A, B). Furthermore, quantification of mitochondrial
494 mass with MitoTracker revealed a reduction only at P2 ($p=0.0005$, $n\geq 10$) in IR pups (Figure 2C
495 and Supplementary Figure 3C-E). Additionally, quantification of TUNEL staining in midline sagittal
496 sections of the cerebella showed a large increase in cell death in the EGL of injured cerebella at
497 P2 ($p=0.0040$, $n=4$), but not at P3 compared to the controls (Figure 2D, E; see also Figure 3K, L).
498 Outside the EGL there was a small increase in cell death after injury that was only significant at
499 P3 ($p=0.0379$, $n\geq 3$) (Figure 2F, G). Thus, a transient increase in ROS in the cerebellum one day
500 after irradiation at P1 correlates with the timing of the major death of GCPs.

501

502 **Altered glial microenvironment following death of granule cell precursors**

503

504 Given the potential importance of glial cells to regenerative cellular responses after injury, we next
505 asked whether the glial microenvironment of the cerebellum changes during early postnatal
506 development in response to irradiation at P1. We first analyzed the astrocyte marker GFAP, since
507 it is generally upregulated soon after brain injury (Burda and Sofroniew, 2014). Most astrocytes,
508 including the specialized Bg, express GFAP in the adult cerebellum, but the cells are generated
509 by gliogenic-NEPs during the first two weeks after birth in mice. We therefore determined the
510 normal location and timing of initiation of GFAP expression in these cells during postnatal
511 cerebellum development. GFAP was first detected in rare astrocytes at P2 located in the white
512 matter (WM) below the lobules, with strong expression in all WM astrocytes at P5 and later stages
513 (P8 and P12) (Figure 3A-D, observed in $n=4$ mice/stage). In contrast, GFAP expression in
514 astrocytes in the developing IGL and in the glial processes of Bg that project through the molecular
515 layer (ML) and EGL was not detectable until P5 and was much stronger at P8 and P12 (Figure
516 3A-D). Interestingly, after injury at birth, GFAP expression was prematurely upregulated in the
517 WM astrocytes below the lobules at P2 and in the remaining astrocytes at P5, including in the
518 fibers of Bg that extend through the ML and EGL, compared to nonIR cerebella (Figure 3A-H,
519 observed in $n=4$ mice/stage). GFAP expression was similar in all glia in both conditions at P8 and
520 P12. These results reveal that astrocytes and Bg react to EGL injury caused by irradiation at P1
521 by initiating GFAP expression earlier than normal in the deep WM, and then the IGL and in Bg.

522

523 The macrophages of the brain, microglia, are generated in the early embryo but their main
524 increase in cell number occurs during neonatal development in mice (Hammond et al., 2018). We
525 found that nearly all microglia were located in the WM of the cerebellum, and that the density of
526 IBA1+ microglia in the WM increased between P2 (235.1 ± 18.3 cells/mm²) and P3 (344.3 ± 53.1
527 cells/mm²) and then was maintained at P5 (350.4 ± 40.2 cells/mm²) (Fig. 3I-K, Supplementary
528 Figure 3F). Since the area of the cerebellum is increasing between P2 and P5, active microglia
529 production and/or infiltration must continue to occur between P2 and P5. As expected, after
530 irradiation the density of microglia in the injured EGL was significantly increased (~3 fold) at P2
531 but not at P3 or P5 compared to controls ($p=0.0331$, $n=4$) (Fig. 3L-N, Supplementary Figure 3G).
532 No difference in the microglial density in the WM was detected between conditions at both time
533 points (Fig. 3I-L; Supplementary Figure 3F). Thus, as expected microglia density was increased
534 in the EGL one day after injury when the maximum GCP cell death occurs.

535

536 **Decreasing ROS impairs cerebellar repair**

537

538 Given the transient increase in ROS signaling in gliogenic-NEPs during peak GCP death and
539 recruitment of microglia to the EGL, and the later astroglial response, we tested whether an
540 increase in ROS is necessary for adaptive reprogramming and cerebellar repair following EGL
541 injury at P1. To reduce the level of ROS we utilized an *mCAT* transgenic mouse line that
542 expresses the human mitochondrial catalase ubiquitously from a *CMV* promoter (Schriner et al.,
543 2005). The transgene is expected to reduce mitochondrial ROS levels in all cells by catalyzing
544 the breakdown of hydrogen peroxide into water and oxygen, hence protecting the cells from
545 oxidative damage. We confirmed that mCAT protein is expressed throughout the cerebellum
546 using immunohistochemical (IHC) staining of cerebellar sections (Figure 4A, B). MitoSOX flow
547 cytometry revealed a significant decrease in ROS in the cerebella of *mCAT*^{+/+} mice 1 day after
548 irradiation (P2) ($p=0.0163$, $n \geq 8$) and not at P3 or P5 compared to control IR mice and no baseline
549 decrease in ROS at any stage in nonIR mice (Figure 4C and Supplementary Figure 4A, B).
550 Mitochondrial mass, as measured by MitoTracker flow cytometry, was reduced at P2 in *mCAT*^{+/+}
551 IR compared to nonIR *mCAT*^{+/+} pups with no significant difference observed between *mCAT*^{+/+}
552 and control IR mice (Fig. 4D, Supplementary Figure 4C, D). The level of cell death in the EGL
553 and density of IBA1+ microglia in the EGL and elsewhere in the cerebellum were similar between
554 *mCAT*^{+/+} and littermate control IR mice at P2 and P3 (Fig. 4E, F, Supplementary Figure 4G, J).
555 There was a slight increase in cell death outside the EGL at P2 in IR *mCAT*^{+/+} compared to nonIR
556 *mCAT*^{+/+} mice but not compared to IR controls (Supplementary Figure 4F, E). Thus, the *mCAT*

557 transgene counteracts the transient increase in cerebellar ROS following EGL injury but does
558 have a major effect on GCP death or the infiltration of microglia to the injured EGL (Supplementary
559 Figure 4 F-J).

560

561 We next determined the regenerative efficiency of *mCAT/+* mice by analyzing the area of sections
562 of cerebella from nonIR and IR P30 *mCAT/+* mice compared to littermate controls. Strikingly, the
563 cross-sectional area of the medial cerebellum (vermis) of IR *mCAT/+* adult mice was significantly
564 reduced compared to IR controls ($p=0.0040$, $n\geq 6$) (Fig. 4G-K). Analysis of cerebellar area across
565 ages (P3, 5, 8 and 12) revealed that the vermis sectional area of the IR *mCAT/+* cerebella was
566 only significantly reduced at P30 compared to IR controls, however at P12 it was reduced in
567 *mCAT/+* IR cerebella compared to *mCAT/+* nonIR mice, whereas it was not significantly different
568 between control IR and control nonIR mice (Fig. 4L, Supplementary Figure 4 K-N). These results
569 indicate that cerebellar growth begins to be reduced at P12 in *mCAT/+* mice following injury. Thus,
570 a reduction in ROS at the time of cell death in the EGL leads to a diminution of cerebellar recovery.

571

572 **Reduced regeneration in *mCAT* mice is associated with reduced adaptive reprogramming**
573 **at P5.**

574

575 Given that a decrease in ROS following EGL injury reduces regeneration of the neonatal
576 cerebellum, we determined whether specific stages of the adaptive reprogramming process are
577 altered in *mCAT/+* mice compared to controls. First, we analyzed the replenishment of the EGL
578 by BgL-NEPs in vermis lobules 3-5, since our previous work showed that these lobules have a
579 prominent defect. Interestingly, we found that although the thickness of the EGL in IR mice of both
580 genotypes was similarly reduced compared to nonIR mice at P5 ($p=0.0041$ control and $p=0.0005$
581 *mCAT/+*; $n\geq 4$) by P8 the control EGL was a similar thickness to the control nonIR whereas the
582 thickness of the *mCAT/+* IR EGL was significantly reduced compared to *mCAT/+* nonIR mice
583 ($p=0.035$, $n=4$) (Figure 5A, B). A key regenerative process that contributes to the expansion of the
584 EGL following injury is the migration of BgL-NEPs to the EGL. Strikingly, the density of CFP+ cells
585 in the EGL (mainly BgL-derived NEPs) was significantly decreased in *mCAT/+* IR mice compared
586 to control IR mice at P5 ($p=0.0002$, $n=4$) but not P3 (Figure 5C-G, Supplementary Figure 5A).
587 Furthermore, the density of NEPs (CFP+ or SOX2+ cells) in the BgL was significantly decreased
588 at P5 in *mCAT/+* IR cerebella compared to controls ($p=0.0010$, $n\geq 5$) but not at other stages (Figure
589 5H, Supplementary Figure 5B-D). These results indicate that BgL-NEPs have a blunted response
590 to EGL injury, and therefore do not fully expand and contribute to the replenishment of GCPs in
591 the EGL after irradiation.

592

593 **Microglia likely contribute to one aspect of adaptive reprogramming.**

594 Given that several steps in adaptive reprogramming were decreased specifically at P5 in *mCAT/+*
595 IR cerebella, we asked whether microglia/macrophages could be involved in any of the processes.
596 We first determine the density of IBA1+ cells in the EGL and WM of vermis lobules 3-5 at P5 in
597 nonIR and IR mice of both genotypes. As expected, the density of microglia in the EGL was very
598 low in the nonIR control and *mCAT/+* cerebella (Figure 6A-E). Interestingly, whereas control IR
599 mice had a similar number of IBA1+ cells in the WM as nonIR mice of both genotypes at P5, the
600 *mCAT/+* IR mice had a lower density of microglia/macrophages in the WM compared to control
601 IR mice at P5 ($p=0.0012$, $n\geq 3$) (Figure 6A-D, F). This result raised the question of whether
602 macrophages/microglia play a role in adaptive reprogramming.

603

604 We, therefore, tested whether reducing the density of IBA1+ microglia/macrophages after birth
605 would alter adaptive reprogramming at P5 or cerebellar regeneration at later stages. Since
606 macrophages and cerebellar microglia are dependent on colony stimulating factor 1 (CSF1) for
607 their survival, we administered PLX5622, a small molecule inhibitor of CSF receptor 1 (CSFR1),
608 to pups every day from P0-5 (PLX treatment) (Kana et al., 2019, Tan et al., 2021). As expected,
609 IBA1+ cells were significantly decreased in the cerebellum of PLX-treated mice at P5 compared
610 to their controls, both nonIR and IR ($p=0.0015$ and $p=0.0059$, $n=3$ and $n=5$, respectively) (Figure
611 6G, Supplementary Figure 6B-E). The thickness of the EGL was not significantly altered at P5 in
612 PLX-treated IR mice compared to IR controls (Figure 6H). Interestingly, similar to *mCAT/+* mice,
613 the density of Nes-CFP+ cells in the EGL was significantly decreased in PLX-treated IR mice
614 compared to IR controls at P5 ($p=0.0008$, $n=5$) (Figure 6I-M). In contrast, the density of SOX2+
615 cells in the BgL, corresponding to the gliogenic BgL-NEPs, were unchanged in the PLX-treated
616 and control mice, whether irradiated or not, suggesting that the decrease in expansion of BgL-
617 NEPs caused by ROS is not mediated by microglia (Supplementary Figure 6F). When mice were
618 treated with PLX from P0-8 and allowed to age to P30, we found the cerebellar vermis section
619 area was not decreased in PLX-treated IR mice compared to IR controls (Figure 6N). Thus,
620 reducing the density of IBA1+ microglia/macrophages in neonatal mice reduces the recruitment
621 of Nes-CFP+ cells to the EGL at P5, but does not have a long-term significant impact on
622 regeneration of the cerebellum.

623

624 **Discussion**

625 We demonstrate that a transient increase in ROS signaling after cerebellar injury to the EGL is
626 critical for adaptive reprogramming and full recovery of cerebellar growth. ROS likely acts as an
627 alarm signal shortly after injury. scRNA-seq at P1-5 and bulk ATAC-seq at P2 of NEPs following
628 targeted irradiation at P1 revealed a rapid increase in transcriptional and epigenetic changes
629 associated with upregulation of ROS and stress related pathways in NEPs that peaked at P2. A
630 transient upregulation in ROS at P2 was confirmed using flow cytometry and found to correlate
631 with the timing of cell death in the EGL one day after irradiation. By reducing mitochondrial ROS
632 levels across all cell types at P2 using an *mCAT* transgene, we uncovered that ROS is required
633 for several steps of adaptive reprogramming of BgLN-NEPs. In addition, we found that microglia
634 are reduced in injured *mCAT*/⁺ pups, which is consistent with prior evidence that ROS can trigger
635 immune cell recruitment in other systems (Kim et al., 2010, Mehl et al., 2022). Moreover,
636 temporary depletion of microglia caused a reduction in the number of NEPs that migrate into the
637 EGL at P5 following injury at P1, but no long-term reduction of cerebellar size. Thus, we identified
638 key transcriptomic and epigenomic changes in cerebellar NEPs upon GCP ablation at birth and
639 discovered roles for the tissue microenvironment, especially ROS and a more limited role of
640 microglia during neonatal cerebellum regeneration.

641
642 scRNA-seq analysis of NEPs from nonIR (P1-3, P5) and nonIR (P2, P3, P5) showed an increase
643 in genes associated with stress responses after irradiation in both the gliogenic and neurogenic
644 subpopulations, but not in the GCPs. Furthermore, an increase in ROS signaling was detected
645 one day after injury (P2) in all three lineages. The injury-induced ROS and stress-related gene
646 signatures were not observed in the later P3+5 gliogenic- and neurogenic-NEPs, suggesting that
647 the increase in ROS levels is an early injury induced signal affecting the NEP transcriptome. Our
648 bulk ATAC-seq data generated at P2 revealed that the open chromatin regions in the IR NEPs
649 were enriched for transcription factor binding motifs related to ROS signaling and stress induced
650 transcription factors such as FOXO3 and AP1 (Table S6). Thus, cerebellar injury during
651 development induces transcriptional and epigenomic signatures in the NEPs and ROS signaling
652 could be a key driver of NEP adaptive reprogramming. Our results are in line with other
653 regeneration systems where a temporary increase in ROS is observed upon cell death or injury
654 and is considered to be a DAMP (Niethammer, 2016).

655
656 Interestingly, although both gliogenic- and neurogenic-NEPs showed induction of cellular stress
657 related genes upon injury, upregulation of ROS signaling and related genes appeared greater in
658 the *Hopx*-expressing gliogenic NEPs that undergo adaptive reprogramming. Whether the

659 upregulation of ROS signaling in the BgL-NEPs is due to BgL-NEPs being in proximity to the dying
660 GCPs after injury or their direct contact due to their radial projections remains to be determined.
661 The ability of BgL-NEPs to respond to GCP death via upregulating ROS signaling and impaired
662 regeneration upon reduction of ROS levels, shows that ROS signaling is involved in triggering
663 adaptive reprogramming upon injury.

664

665 The cellular composition of the neonatal cerebellum is dramatically different from the adult. During
666 the early postnatal period, we found that astrocytes in the WM below the lobules are the first to
667 initiate GFAP expression at P2 and that by P5 all astrocytes express a high level of GFAP. In
668 contrast, Bg express a low level of GFAP at P5 and reach a high level by P8. Interestingly, we
669 found that injury leads to an increase in the level of GFAP expression in each type of astroglia
670 when they first initiate expression, deep WM astrocytes at P2 and Bg (and all astrocytes) at P5.
671 Once adaptive reprogramming is nearing completion (P8), the GFAP levels remained similar in
672 all astroglia in nonIR and IR cerebella. These results suggest that the neonatal astrocytes respond
673 to injury differently than in the adult where GFAP upregulation is observed immediately after injury
674 (Burda and Sofroniew, 2014), since Bg and astrocytes in the lobules have a delayed response to
675 injury with GFAP not being upregulated for several days. Furthermore, at birth the microglia have
676 not fully expanded in number in the cerebellum and previous scRNA-seq showed that the
677 neonatal and adult microglia are transcriptionally distinct (Hammond et al., 2019). Perhaps
678 neonatal microglia are anti-inflammatory and pro-regenerative upon injury in neonates, in contrast
679 to adult microglia where upon traumatic brain injury they can inhibit regeneration (Donat et al.,
680 2017). Collectively, the differences in glial responses to injury in the neonatal cerebellum and
681 adult brain likely contributes to the permissiveness of the neonatal cerebellum to regeneration.
682 Details of the molecular changes that the neonatal cerebellar microglia/macrophages and
683 astrocytes undergo upon GCP injury and their molecular crosstalk with NEPs remain to be
684 determined.

685

686 We demonstrated the significance of ROS activation in the NEP reprogramming process using
687 an *mCAT* transgenic mouse line in which human Catalase (CAT) is expressed in mitochondria, a
688 protein that can lead to a reduction in hydrogen peroxide (H₂O₂) and thus lower ROS. However,
689 in *mCAT* neonatal cerebella we found that the percentage of MitoSOX high cells are comparable
690 to control mice under nonIR conditions. Importantly, however, one day after irradiation at P1 when
691 the percentage of MitoSOX high cells increases in control IR mice, the *mCAT* transgene reduces
692 the percentage of MitoSOX high cells, such that it remains at the baseline nonIR *mCAT* level.

693 Therefore, human CAT expression in mitochondria in this model inhibits the injury-induced
694 increase in ROS levels without affecting the homeostatic production of superoxide. Of possible
695 relevance, in this mouse model the observed change in ROS levels is likely global, impacting all
696 cell types. The specific impact of increased mCAT in BgL-NEPs or microglia on their recruitment
697 and function after an injury remains to be determined with new cell type-specific tools.

698

699 Our experiments depleting microglia using PLX5622 indicate that microglia/macrophages are
700 involved in the regeneration of the EGL following irradiation. Previous studies have demonstrated
701 a dual role of microglia in promoting and inhibiting regenerative processes within the nervous
702 system (Lee et al., 2021, Wang et al., 2020). Our data support the idea that microglia are involved
703 in the adaptive reprogramming of NEPs to GCPs by promoting their replenishment of GCPs in
704 the EGL. While the direct mechanisms remain to be discovered, given the small size of the lobules
705 and disruption of the cytoarchitecture after injury it might be possible for secreted factors from the
706 white matter microglia to reach the BgL NEPs. Alternatively, there could be a relay system through
707 an intermediate cell type closer to the microglia. PLX-treatment for 8 days after irradiation did not
708 reduce the later growth of the injured cerebellum. One possibility is that after the cessation of PLX
709 administration, regeneration proceeds normally. Additionally, regenerative processes that act in
710 parallel to microglial signaling are likely required.

711

712 Collectively, we have delineated the spatiotemporal cellular changes in the cerebellar glial
713 microenvironment upon ablation of GCPs at birth and highlight ROS signaling as a key stimulator
714 of adaptive reprogramming of NEPs. The details of how DAMP-glia-progenitor crosstalk is
715 orchestrated remains to be untangled. Understanding how microenvironmental responses shape
716 repair processes is a crucial first step towards developing strategies to promote regeneration.

717

718 **Acknowledgements**

719 We thank past and present members of the Joyner laboratory for discussions and technical help.
720 We would like to thank Dr Ronan Chaligne and his team for their support in the multiplexed
721 scRNA-seq experiments. We are grateful to the MSKCC Animal Imaging Core, Flow cytometry
722 Core, Center for Comprehensive Medicine and Pathology, Integrated Genomics Operation,
723 Single-cell Analytics and Innovation Laboratory and Epigenetics Computational Laboratory teams
724 for technical services and support. An XRad 225Cx Microirradiator was purchased by support
725 from a Shared Resources Grant from the MSKCC Geoffrey Beene Cancer Research Center. We
726 gratefully acknowledge the support of the Gurdon Institute Scientific Computing Facility.

727

728 This work was supported by grants from the NIH to ALJ (R01NS092096) and NSB (NINDS K99
729 NS112605-01). Additional funding was provided to ALJ from an NCI Cancer Center Support Grant
730 (CCSG, P30 CA08748) and the Cycle for Survival, to SEN from a Francois Wallace Monahan
731 Fellowship; to NSB from a Wellcome Career Development Award (227294/Z/23/Z), Royal Society
732 grant (RGS\R1\231143) and Cambridge Stem Cell Institute Seed Funding, and to JBC from a
733 University of Cambridge School of Biological Sciences DTP PhD Studentship and Peter and
734 Emma Thomsen's Scholarship (1051). Gurdon Institute is supported by a Wellcome Core Grant
735 (203144) and CRUK Grant (C6946/A24843).

736

737

738 **References:**

- 739
- 740 ALTMAN, J. & ANDERSON, W. J. 1971. Irradiation of the cerebellum in infant rats with low-level
741 x-ray: histological and cytological effects during infancy and adulthood. *Exp Neurol*, 30,
742 492-509.
- 743 ALTMAN, J. & BAYER, S. A. 1997. *Development of the cerebellar system in relation to its*
744 *evolution, structure, and functions*, Boca Raton, CRC Press.
- 745 AUTEN, R. L. & DAVIS, J. M. 2009. Oxygen Toxicity and Reactive Oxygen Species: The Devil
746 Is in the Details. *Pediatric Research*, 66, 121-127.
- 747 BADURA, A., VERPEUT, J. L., METZGER, J. W., PEREIRA, T. D., PISANO, T. J., DEVERETT,
748 B., BAKSHINSKAYA, D. E. & WANG, S. S. 2018. Normal cognitive and social
749 development require posterior cerebellar activity. *Elife*, 7.
- 750 BAYIN N. S., M. D., STEPHEN N. D., LAO Z., SIMS P. A., JOYNER A. L. 2021. Injury induced
751 ASCL1 expression orchestrates a transitory cell state required for repair of the neonatal
752 cerebellum. *Sci Adv*, 7, eabj1598.
- 753 BAYIN, N. S., WOJCINSKI, A., MOURTON, A., SAITO, H., SUZUKI, N. & JOYNER, A. L. 2018.
754 Age-dependent dormant resident progenitors are stimulated by injury to regenerate
755 Purkinje neurons. *Elife*, 7.
- 756 BENSELLAM, M., CHAN, J. Y., LEE, K., JOGLEKAR, M. V., HARDIKAR, A. A., LOUDOVARIS,
757 T., THOMAS, H. E., JONAS, J. C. & LAYBUTT, D. R. 2019. Phlda3 regulates beta cell
758 survival during stress. *Sci Rep*, 9, 12827.
- 759 BIGARELLA, C. L., LIANG, R. & GHAFARI, S. 2014. Stem cells and the impact of ROS
760 signaling. *Development*, 141, 4206-18.
- 761 BROWN, A. M., WHITE, J. J., VAN DER HEIJDEN, M. E., ZHOU, J., LIN, T. & SILLITOE, R. V.
762 2020. Purkinje cell misfiring generates high-amplitude action tremors that are corrected
763 by cerebellar deep brain stimulation. *Elife*, 9.
- 764 BUCKNER, R. L. 2013. The cerebellum and cognitive function: 25 years of insight from anatomy
765 and neuroimaging. *Neuron*, 80, 807-15.
- 766 BURDA, J. E. & SOFRONIEW, M. V. 2014. Reactive gliosis and the multicellular response to
767 CNS damage and disease. *Neuron*, 81, 229-48.
- 768 CERRATO, V., PARMIGIANI, E., FIGUERES-ONATE, M., BETIZEAU, M., APRATO, J.,
769 NANAVATY, I., BERCHIALLA, P., LUZZATI, F., DE'SPERATI, C., LOPEZ-
770 MASCARAQUE, L. & BUFFO, A. 2018. Multiple origins and modularity in the
771 spatiotemporal emergence of cerebellar astrocyte heterogeneity. *PLoS Biol*, 16,
772 e2005513.
- 773 CLUTTON, G., MOLLAN, K., HUDGENS, M. & GOONETILLEKE, N. 2019. A Reproducible,
774 Objective Method Using MitoTracker® Fluorescent Dyes to Assess Mitochondrial Mass
775 in T Cells by Flow Cytometry. *Cytometry A*, 95, 450-456.
- 776 CORCES, M. R., TREVINO, A. E., HAMILTON, E. G., GREENSIDE, P. G., SINNOTT-
777 ARMSTRONG, N. A., VESUNA, S., SATPATHY, A. T., RUBIN, A. J., MONTINE, K. S.,
778 WU, B., KATHIRIA, A., CHO, S. W., MUMBACH, M. R., CARTER, A. C., KASOWSKI,
779 M., ORLOFF, L. A., RISCA, V. I., KUNDAJE, A., KHAVARI, P. A., MONTINE, T. J.,
780 GREENLEAF, W. J. & CHANG, H. Y. 2017. An improved ATAC-seq protocol reduces
781 background and enables interrogation of frozen tissues. *Nature Methods*, 14, 959-962.
- 782 CORRALES, J. D., BLAESS, S., MAHONEY, E. M. & JOYNER, A. L. 2006. The level of sonic
783 hedgehog signaling regulates the complexity of cerebellar foliation. *Development*, 133,
784 1811-21.
- 785 DE LUCA, A., PARMIGIANI, E., TOSATTO, G., MARTIRE, S., HOSHINO, M., BUFFO, A.,
786 LETO, K. & ROSSI, F. 2015. Exogenous Sonic hedgehog modulates the pool of
787 GABAergic interneurons during cerebellar development. *Cerebellum*, 14, 72-85.

- 788 DEVCHAND, P. R., ZIOUZENKOVA, O. & PLUTZKY, J. 2004. Oxidative Stress and
789 Peroxisome Proliferator–Activated Receptors. *Circulation Research*, 95, 1137-1139.
- 790 DOBBING, J. & SANDS, J. 1973. Quantitative growth and development of human brain. *Arch*
791 *Dis Child*, 48, 757-67.
- 792 DONAT, C. K., SCOTT, G., GENTLEMAN, S. M. & SASTRE, M. 2017. Microglial Activation in
793 Traumatic Brain Injury. *Front Aging Neurosci*, 9, 208.
- 794 ENCINAS, J. M., VAAHTOKARI, A. & ENIKOLOPOV, G. 2006. Fluoxetine targets early
795 progenitor cells in the adult brain. *Proc Natl Acad Sci U S A*, 103, 8233-8.
- 796 FILOSTO, M., TONIN, P., VATTEMI, G., SAVIO, C., RIZZUTO, N. & TOMELLERI, G. 2003.
797 Transcription factors c-Jun/activator protein-1 and nuclear factor-kappa B in oxidative
798 stress response in mitochondrial diseases. *Neuropathol Appl Neurobiol*, 29, 52-9.
- 799 FRANKISH, A., DIEKHANS, M., JUNGREIS, I., LAGARDE, J., LOVELAND, J. E., MUDGE, J.
800 M., SISU, C., WRIGHT, J. C., ARMSTRONG, J., BARNES, I., BERRY, A., BIGNELL, A.,
801 BOIX, C., CARBONELL SALA, S., CUNNINGHAM, F., DI DOMENICO, T.,
802 DONALDSON, S., FIDDES, I. T., GARCIA GIRON, C., GONZALEZ, J. M., GREGO, T.,
803 HARDY, M., HOURLIER, T., HOWE, K. L., HUNT, T., IZUOGU, O. G., JOHNSON, R.,
804 MARTIN, F. J., MARTINEZ, L., MOHANAN, S., MUIR, P., NAVARRO, F. C. P.,
805 PARKER, A., PEI, B., POZO, F., RIERA, F. C., RUFFIER, M., SCHMITT, B. M.,
806 STAPLETON, E., SUNER, M. M., SYCHEVA, I., USZCZYNSKA-RATAJCZAK, B.,
807 WOLF, M. Y., XU, J., YANG, Y. T., YATES, A., ZERBINO, D., ZHANG, Y.,
808 CHOUDHARY, J. S., GERSTEIN, M., GUIGO, R., HUBBARD, T. J. P., KELLIS, M.,
809 PATEN, B., TRESS, M. L. & FLICEK, P. 2021. Gencode 2021. *Nucleic Acids Res*, 49,
810 D916-D923.
- 811 FRIK, J., MERL-PHAM, J., PLESNILA, N., MATTUGINI, N., KJELL, J., KRASKA, J., GOMEZ,
812 R. M., HAUCK, S. M., SIRKO, S. & GOTZ, M. 2018. Cross-talk between monocyte
813 invasion and astrocyte proliferation regulates scarring in brain injury. *EMBO Rep*, 19.
- 814 HAGENBUCHNER, J., KUZNETSOV, A., HERMANN, M., HAUSOTT, B., OBEXER, P. &
815 AUSSERLECHNER, M. J. 2012. FOXO3-induced reactive oxygen species are regulated
816 by BCL2L11 (Bim) and SESN3. *J Cell Sci*, 125, 1191-203.
- 817 HAMMOND, T. R., DUFORT, C., DISSING-OLESEN, L., GIERA, S., YOUNG, A., WYSOKER,
818 A., WALKER, A. J., GERGITS, F., SEGEL, M., NEMESH, J., MARSH, S. E.,
819 SAUNDERS, A., MACOSKO, E., GINHOUX, F., CHEN, J., FRANKLIN, R. J. M., PIAO,
820 X., MCCARROLL, S. A. & STEVENS, B. 2019. Single-Cell RNA Sequencing of Microglia
821 throughout the Mouse Lifespan and in the Injured Brain Reveals Complex Cell-State
822 Changes. *Immunity*, 50, 253-271 e6.
- 823 HAMMOND, T. R., ROBINSON, D. & STEVENS, B. 2018. Microglia and the Brain:
824 Complementary Partners in Development and Disease. *Annu Rev Cell Dev Biol*, 34,
825 523-544.
- 826 HAO, Y., HAO, S., ANDERSEN-NISSEN, E., MAUCK, W. M., 3RD, ZHENG, S., BUTLER, A.,
827 LEE, M. J., WILK, A. J., DARBY, C., ZAGER, M., HOFFMAN, P., STOECKIUS, M.,
828 PAPALEXI, E., MIMITOU, E. P., JAIN, J., SRIVASTAVA, A., STUART, T., FLEMING, L.
829 M., YEUNG, B., ROGERS, A. J., MCEL RATH, J. M., BLISH, C. A., GOTTARDO, R.,
830 SMIBERT, P. & SATIJA, R. 2021. Integrated analysis of multimodal single-cell data.
831 *Cell*, 184, 3573-3587 e29.
- 832 JIANG, J., HUANG, Z., ZHAO, Q., FENG, W., BELIKOVA, N. A. & KAGAN, V. E. 2008.
833 Interplay between bax, reactive oxygen species production, and cardiolipin oxidation
834 during apoptosis. *Biochem Biophys Res Commun*, 368, 145-50.
- 835 JOYNER, A. L. & BAYIN, N. S. 2022. Cerebellum lineage allocation, morphogenesis and repair:
836 impact of interplay amongst cells. *Development*, 149.
- 837 KAELIN, W. G. 2005. ROS: Really involved in Oxygen Sensing. *Cell Metabolism*, 1, 357-358.

- 838 KAMINOW, B., YUNUSOV, D. & DOBIN, A. 2021. STARsolo: accurate, fast and versatile
839 mapping/quantification of single-cell and single-nucleus RNA-seq data. *bioRxiv*,
840 2021.05.05.442755.
- 841 KANA, V., DESLAND, F. A., CASANOVA-ACEBES, M., AYATA, P., BADIMON, A., NABEL, E.,
842 YAMAMURO, K., SNEEBOER, M., TAN, I. L., FLANIGAN, M. E., ROSE, S. A., CHANG,
843 C., LEADER, A., LE BOURHIS, H., SWEET, E. S., TUNG, N., WROBLEWSKA, A.,
844 LAVIN, Y., SEE, P., BACCARINI, A., GINHOUX, F., CHITU, V., STANLEY, E. R.,
845 RUSSO, S. J., YUE, Z., BROWN, B. D., JOYNER, A. L., DE WITTE, L. D., MORISHITA,
846 H., SCHAEFER, A. & MERAD, M. 2019. CSF-1 controls cerebellar microglia and is
847 required for motor function and social interaction. *J Exp Med*, 216, 2265-2281.
- 848 KIM, D., YOU, B., JO, E. K., HAN, S. K., SIMON, M. I. & LEE, S. J. 2010. NADPH oxidase 2-
849 derived reactive oxygen species in spinal cord microglia contribute to peripheral nerve
850 injury-induced neuropathic pain. *Proc Natl Acad Sci U S A*, 107, 14851-6.
- 851 KOWALCZYK, M. S., TIROSH, I., HECKL, D., RAO, T. N., DIXIT, A., HAAS, B. J.,
852 SCHNEIDER, R. K., WAGERS, A. J., EBERT, B. L. & REGEV, A. 2015. Single-cell
853 RNA-seq reveals changes in cell cycle and differentiation programs upon aging of
854 hematopoietic stem cells. *Genome Res*, 25, 1860-72.
- 855 LEE, J. W., CHUN, W., LEE, H. J., KIM, S. M., MIN, J. H., KIM, D. Y., KIM, M. O., RYU, H. W. &
856 LEE, S. U. 2021. The Role of Microglia in the Development of Neurodegenerative
857 Diseases. *Biomedicines*, 9.
- 858 LETO, K., ARANCILLO, M., BECKER, E. B., BUFFO, A., CHIANG, C., DING, B., DOBYNS, W.
859 B., DUSART, I., HALDIPUR, P., HATTEN, M. E., HOSHINO, M., JOYNER, A. L., KANO,
860 M., KILPATRICK, D. L., KOIBUCHI, N., MARINO, S., MARTINEZ, S., MILLEN, K. J.,
861 MILLNER, T. O., MIYATA, T., PARMIGIANI, E., SCHILLING, K., SEKERKOVA, G.,
862 SILLITOE, R. V., SOTELO, C., UESAKA, N., WEFERS, A., WINGATE, R. J. &
863 HAWKES, R. 2015. Consensus Paper: Cerebellar Development. *Cerebellum*.
- 864 LI, Q., CHENG, Z., ZHOU, L., DARMANIS, S., NEFF, N. F., OKAMOTO, J., GULATI, G.,
865 BENNETT, M. L., SUN, L. O., CLARKE, L. E., MARSCHALLINGER, J., YU, G., QUAKE,
866 S. R., WYSS-CORAY, T. & BARRES, B. A. 2019. Developmental Heterogeneity of
867 Microglia and Brain Myeloid Cells Revealed by Deep Single-Cell RNA Sequencing.
868 *Neuron*, 101, 207-223 e10.
- 869 LI, Y., HE, X., KAWAGUCHI, R., ZHANG, Y., WANG, Q., MONAVARFESHANI, A., YANG, Z.,
870 CHEN, B., SHI, Z., MENG, H., ZHOU, S., ZHU, J., JACOBI, A., SWARUP, V.,
871 POPOVICH, P. G., GESCHWIND, D. H. & HE, Z. 2020. Microglia-organized scar-free
872 spinal cord repair in neonatal mice. *Nature*, 587, 613-618.
- 873 LOVE, M. I., HUBER, W. & ANDERS, S. 2014. Moderated estimation of fold change and
874 dispersion for RNA-seq data with DESeq2. *Genome Biol*, 15, 550.
- 875 MASGRAS, I., CARRERA, S., DE VERDIER, P. J., BRENNAN, P., MAJID, A., MAKHTAR, W.,
876 TULCHINSKY, E., JONES, G. D. D., RONINSON, I. B. & MACIP, S. 2012. Reactive
877 oxygen species and mitochondrial sensitivity to oxidative stress determine induction of
878 cancer cell death by p21. *J Biol Chem*, 287, 9845-9854.
- 879 MCMAHON, A. P., INGHAM, P. W. & TABIN, C. J. 2003. Developmental roles and clinical
880 significance of hedgehog signaling. *Curr Top Dev Biol*, 53, 1-114.
- 881 MEHL, L. C., MANJALLY, A. V., BOUADI, O., GIBSON, E. M. & TAY, T. L. 2022. Microglia in
882 brain development and regeneration. *Development*, 149.
- 883 NIETHAMMER, P. 2016. The early wound signals. *Curr Opin Genet Dev*, 40, 17-22.
- 884 PARMIGIANI, E., LETO, K., ROLANDO, C., FIGUERES-ONATE, M., LOPEZ-MASCARAQUE,
885 L., BUFFO, A. & ROSSI, F. 2015. Heterogeneity and Bipotency of Astroglial-Like
886 Cerebellar Progenitors along the Interneuron and Glial Lineages. *J Neurosci*, 35, 7388-
887 402.

- 888 QIU, F., CHEN, Y. R., LIU, X., CHU, C. Y., SHEN, L. J., XU, J., GAUR, S., FORMAN, H. J.,
889 ZHANG, H., ZHENG, S., YEN, Y., HUANG, J., KUNG, H. J. & ANN, D. K. 2014. Arginine
890 starvation impairs mitochondrial respiratory function in ASS1-deficient breast cancer
891 cells. *Sci Signal*, 7, ra31.
- 892 RAKIC, P. & SIDMAN, R. L. 1970. Histogenesis of cortical layers in human cerebellum,
893 particularly the lamina dissecans. *J Comp Neurol*, 139, 473-500.
- 894 SALMAN, M. S. & TSAI, P. 2016. The Role of the Pediatric Cerebellum in Motor Functions,
895 Cognition, and Behavior: A Clinical Perspective. *Neuroimaging Clin N Am*, 26, 317-29.
- 896 SCHRINER, S. E., LINFORD, N. J., MARTIN, G. M., TREUTING, P., OGBURN, C. E., EMOND,
897 M., COSKUN, P. E., LADIGES, W., WOLF, N., VAN REMMEN, H., WALLACE, D. C. &
898 RABINOVITCH, P. S. 2005. Extension of murine life span by overexpression of catalase
899 targeted to mitochondria. *Science*, 308, 1909-11.
- 900 SMITH, A. N., SHAUGHNESS, M., COLLIER, S., HOPKINS, D. & BYRNES, K. R. 2022.
901 Therapeutic targeting of microglia mediated oxidative stress after neurotrauma. *Front*
902 *Med (Lausanne)*, 9, 1034692.
- 903 STOODLEY, C. J., D'MELLO, A. M., ELLEGOOD, J., JAKKAMSETTI, V., LIU, P., NEBEL, M.
904 B., GIBSON, J. M., KELLY, E., MENG, F., CANO, C. A., PASCUAL, J. M.,
905 MOSTOFKY, S. H., LERCH, J. P. & TSAI, P. T. 2017. Altered cerebellar connectivity in
906 autism and cerebellar-mediated rescue of autism-related behaviors in mice. *Nat*
907 *Neurosci*, 20, 1744-1751.
- 908 STRICK, P. L., DUM, R. P. & FIEZ, J. A. 2009. Cerebellum and nonmotor function. *Annu Rev*
909 *Neurosci*, 32, 413-34.
- 910 TAN, D. Q. & SUDA, T. 2018. Reactive Oxygen Species and Mitochondrial Homeostasis as
911 Regulators of Stem Cell Fate and Function. *Antioxid Redox Signal*, 29, 149-168.
- 912 TAN, I. L., ARIFA, R. D. N., RALLAPALLI, H., KANA, V., LAO, Z., SANGHRAJKA, R. M.,
913 SUMRU BAYIN, N., TANNE, A., WOJCINSKI, A., KORSHUNOV, A., BHARDWAJ, N.,
914 MERAD, M., TURNBULL, D. H., LAFAILLE, J. J. & JOYNER, A. L. 2021. CSF1R
915 inhibition depletes tumor-associated macrophages and attenuates tumor progression in
916 a mouse sonic Hedgehog-Medulloblastoma model. *Oncogene*, 40, 396-407.
- 917 TOMLINSON, S. P., DAVIS, N. J. & BRACEWELL, R. M. 2013. Brain stimulation studies of non-
918 motor cerebellar function: a systematic review. *Neurosci Biobehav Rev*, 37, 766-89.
- 919 TRAAG, V. A., WALTMAN, L. & VAN ECK, N. J. 2019. From Louvain to Leiden: guaranteeing
920 well-connected communities. *Sci Rep*, 9, 5233.
- 921 TSAI, P. T., RUDOLPH, S., GUO, C., ELLEGOOD, J., GIBSON, J. M., SCHAEFFER, S. M.,
922 MOGAVERO, J., LERCH, J. P., REGEHR, W. & SAHIN, M. 2018. Sensitive Periods for
923 Cerebellar-Mediated Autistic-like Behaviors. *Cell Rep*, 25, 357-367 e4.
- 924 WANG, J., HE, X., MENG, H., LI, Y., DMITRIEV, P., TIAN, F., PAGE, J. C., LU, Q. R. & HE, Z.
925 2020. Robust Myelination of Regenerated Axons Induced by Combined Manipulations of
926 GPR17 and Microglia. *Neuron*, 108, 876-886.e4.
- 927 WANG, S. S., KLOTH, A. D. & BADURA, A. 2014. The cerebellum, sensitive periods, and
928 autism. *Neuron*, 83, 518-32.
- 929 WECHSLER-REYA, R. J. & SCOTT, M. P. 1999. Control of neuronal precursor proliferation in
930 the cerebellum by Sonic Hedgehog [see comments]. *Neuron*, 22, 103-14.
- 931 WOJCINSKI, A., LAWTON, A. K., BAYIN, N. S., LAO, Z., STEPHEN, D. N. & JOYNER, A. L.
932 2017. Cerebellar granule cell replenishment postinjury by adaptive reprogramming of
933 Nestin(+) progenitors. *Nat Neurosci*, 20, 1361-1370.
- 934 ZHENG, G. X., TERRY, J. M., BELGRADER, P., RYVKIN, P., BENT, Z. W., WILSON, R.,
935 ZIRALDO, S. B., WHEELER, T. D., MCDERMOTT, G. P., ZHU, J., GREGORY, M. T.,
936 SHUGA, J., MONTESCLAROS, L., UNDERWOOD, J. G., MASQUELIER, D. A.,
937 NISHIMURA, S. Y., SCHNALL-LEVIN, M., WYATT, P. W., HINDSON, C. M.,
938 BHARADWAJ, R., WONG, A., NESS, K. D., BEPPU, L. W., DEEG, H. J., MCFARLAND,

939 C., LOEB, K. R., VALENTE, W. J., ERICSON, N. G., STEVENS, E. A., RADICH, J. P.,
940 MIKKELSEN, T. S., HINDSON, B. J. & BIELAS, J. H. 2017. Massively parallel digital
941 transcriptional profiling of single cells. *Nat Commun*, 8, 14049.
942
943
944

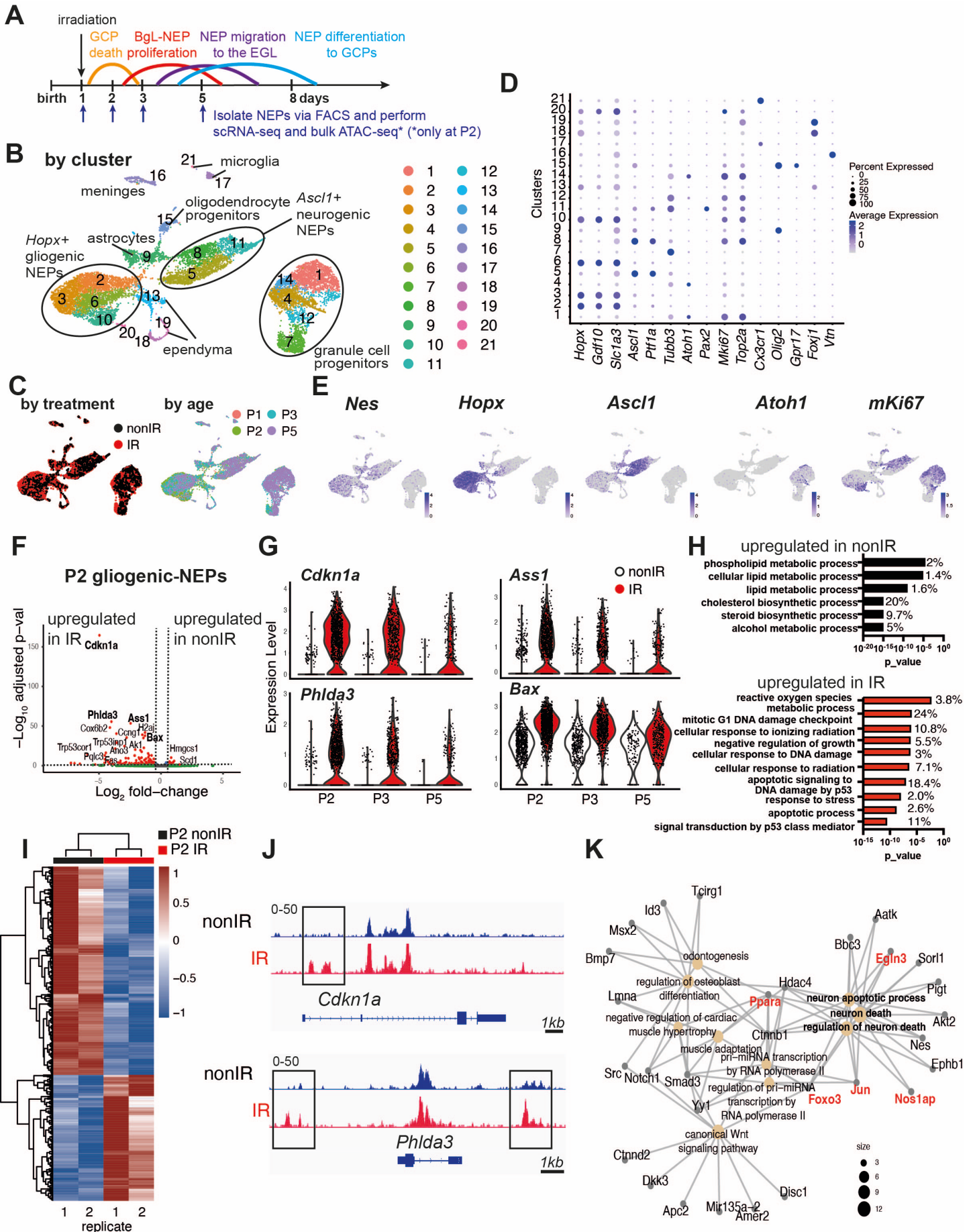


Figure 1: Injury induces ROS and cell stress signaling reflected by changes in the transcriptome and chromatin landscape of progenitors.

(A) Schematic summarizing the experimental plan.

(B-C) UMAP projections of 11,878 cells (6,978 nonIR and 4,900 IR) showing cluster annotations (B), treatment (black: nonIR, red: IR) and the age of the samples (red: P1, green: P2, blue: P3, purple: P5) (C).

(D) Dot plot showing the expression levels of key marker genes used for cluster annotation (gliogenic-NEPs: *Hopx*, *Gdf10*, *Slc1a3*, neurogenic-NEPs: *Ascl1*, *Ptf1a*, immature neurons: *Pax2*, GCPs: *Atoh1*, postmitotic neurons: *Tubb3*, microglia: *Cx3cr1*, oligodendrocyte progenitors: *Olig2*, oligodendrocytes: *Gpr17*, Ependymal cells: *Foxj1*).

(E) Feature plots showing *Nes*, *Hopx* (gliogenic-NEPs), *Ascl1* (neurogenic-NEPs) and *Atoh1* (GCPs) and *mKi67* (proliferation) expression highlighting the three main populations of interest. Clusters containing *Hopx*-NEPs (clusters 2, 3, 6, 10), *Ascl1*-NEPs (clusters 5, 8, 11), or GCPs (clusters 1, 4, 7, 12, 14) were subsetted from the original data set and were divided according to age (P2 or P3+P5) for the downstream differential expression analyses.

(F) Volcano plot showing differentially expressed genes in the P2 gliogenic-NEPs (red: adjusted p-value \leq 0.05, log₂fold-change $>$ |1|).

(G) Violin plots showing some of the top differentially expressed genes in P2 gliogenic-NEPs and how their expression changes over time with respect to their expression in control cells.

(H) Some of the significant GO terms associated with differentially expressed genes in P2 gliogenic-NEPs that were either upregulated in nonIR (top panel) or IR (bottom panel) cells (adjusted p-value \leq 0.05, Table S3).

(I) Heatmap showing differentially open chromatin regions in P2 nonIR and IR NEPs, identified by bulk ATAC-seq (1168 differentially open regions, adjusted p-value $<$ 0.05, Table S4).

(J) Tracks highlighting the injury-induced open chromatin regions around *Cdkn1a* and *Phlda3*, the top differentially expressed genes identified in (F).

(K) Linkages between genes and GO-terms identified by the ATAC-seq data revealed an active transcriptional network involved in regulating cell death and apoptosis. Genes colored in red (*Ppara*, *Egln3*, *Foxo3*, *Jun* and *Nos1ap*) have been implicated as upregulated with increased ROS levels or involved in ROS signaling.

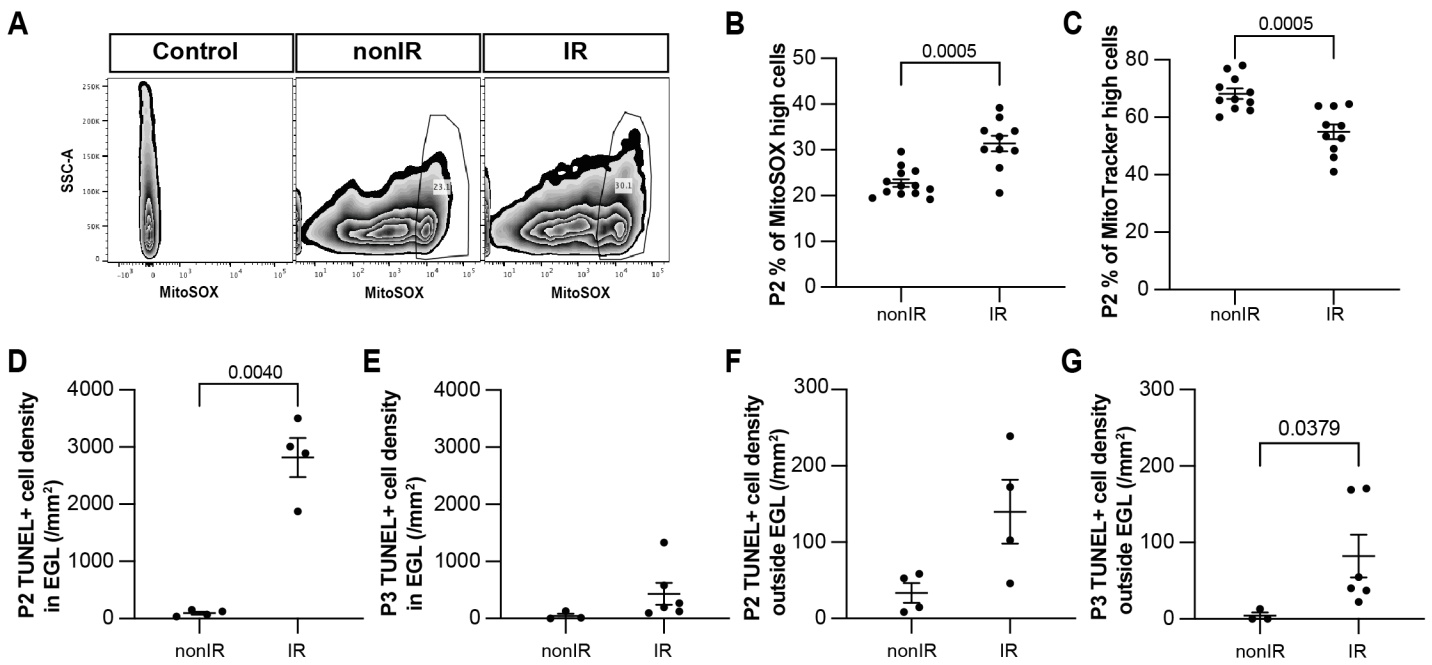


Figure 2: Cerebellar injury at P1 results in increased superoxide production, a reduction in mitochondria and increased cell death in the EGL that peaks 24h after injury.

(A) Examples of flow cytometry analysis of mitochondrial ROS at P2 from nonIR and IR cerebella using MitoSOX dye. Gating determined the top 90% MitoSOX signal (MitoSOX high cells).

(B, C) Quantification of MitoSOX high (B) and MitoTracker high (C) expression in nonIR and IR cerebella at P2.

(D, E) Quantification of TUNEL+ cell density in the EGL at P2 (D) and P3 (E) in lobules 3-5 of nonIR and IR mice.

(F, G) Quantification of TUNEL+ cell density outside the EGL at P2 (F) and P3 (G) in lobules 3-5 of nonIR and IR mice.

EGL, External granular layer; SSC, side scatter; P, postnatal day; nonIR, non-irradiated; IR, irradiated. All statistical significance was determined using an unpaired t-test and data are represented as mean \pm SEM.

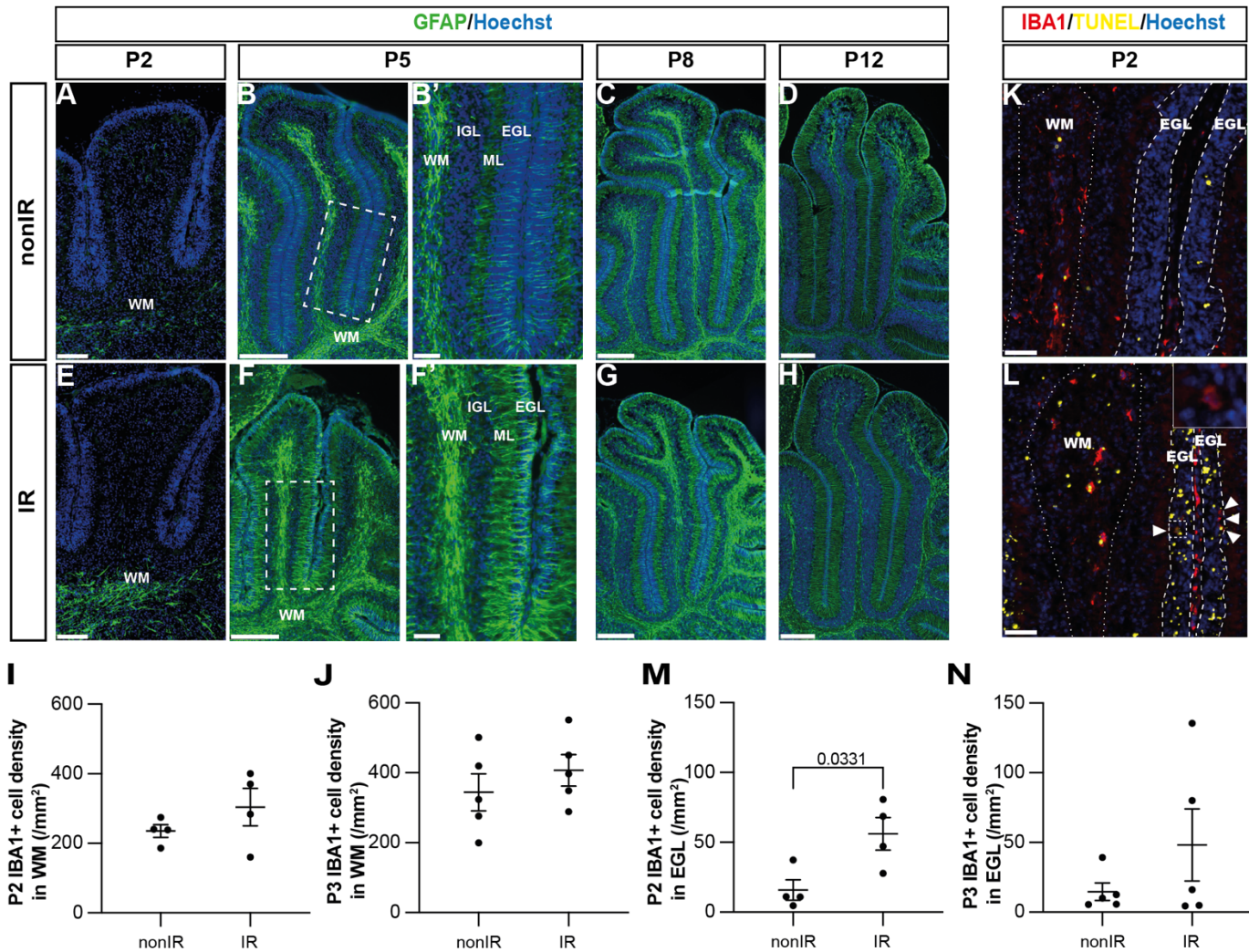


Figure 3: Cerebellar injury at P1 induces transient microglial recruitment to the EGL and prolonged astroglial microenvironment changes in the cerebellum.

(A-H) Immunohistochemical (IHC) staining of medial sagittal cerebellar sections for GFAP (green) in lobules 4/5 of nonIR and IR cerebellum at the stages indicated. Nuclei were counterstained with Hoechst. (B') and (F') show high-power images of white dashed line boxes in (B) and (F), respectively.

(I, J) Quantification of IBA1+ cell density in the WM at P2 (I) and P3 (J) in lobules 3-5 of nonIR and IR mice. (K, L) IHC staining of medial sagittal cerebellar sections for IBA1 and TUNEL in lobule 3 of nonIR and IR cerebellum at P2. Nuclei were counterstained with Hoechst. White matter (WM) and external granular layer (EGL) are delineated by white dotted lines and dashed lines, respectively. High-power image in (L) of the area indicated by the white dashed line represents an IBA1+ cell present in the EGL. White arrowheads indicate additional IBA1+ cells in the EGL.

(M, N) Quantification of IBA1+ cell density in the EGL at P2 (M) and P3 (N) in lobules 3-5 of nonIR and IR mice. EGL, External granular layer; WM, White matter; P, postnatal day; nonIR, non-irradiated; IR, irradiated. Scale bar: A and E 100 μm , B, C, D, E, F, G and H: 250 μm , B' and F': 50 μm , I and J: 50 μm . All statistical significance was determined using an unpaired t-test and data are represented as mean \pm SEM.

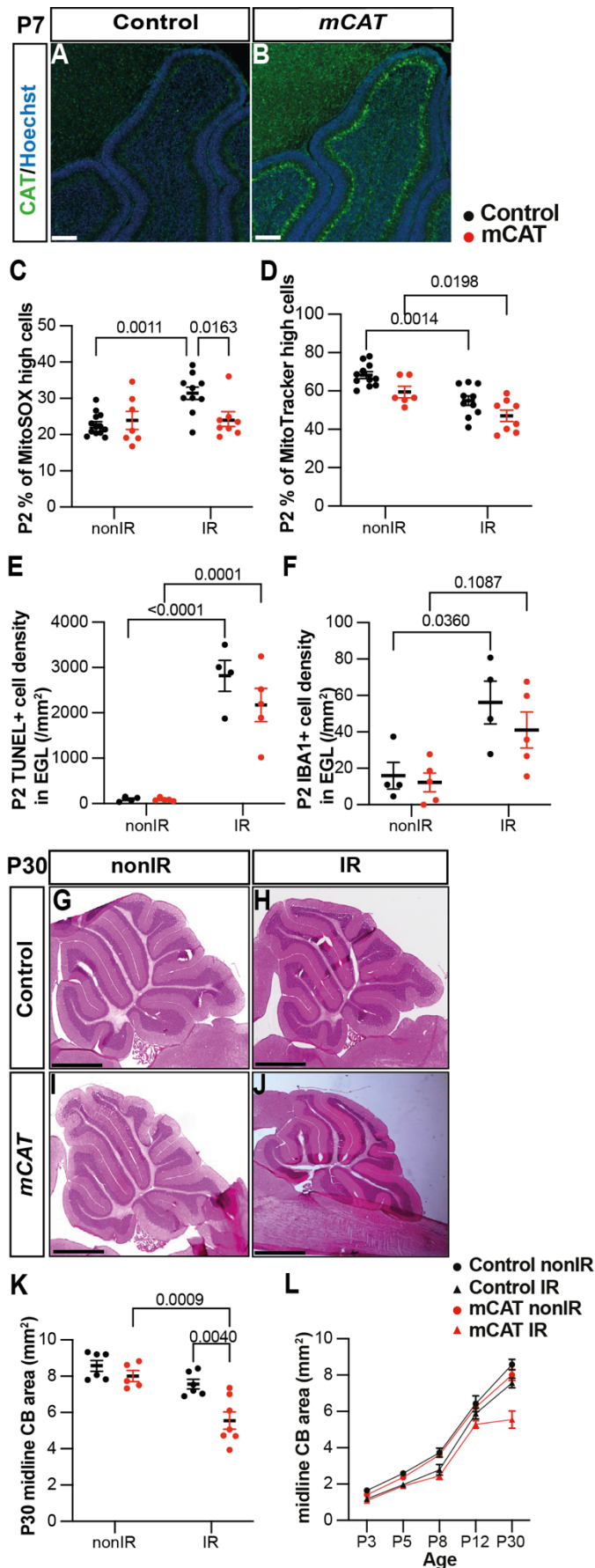


Figure 4: Reduction of ROS impairs adaptive reprogramming and cerebellar repair.

(A, B) IHC staining of medial sagittal cerebellar sections for human catalase in control (A) AND *mCAT*^{+/+} mice (B) at P7. Nuclei were counterstained with Hoechst (blue). Similar staining was seen in four *mCAT*^{+/+} mice.

(C) Quantification of MitoSOX high expression at P2 in control and *mCAT*^{+/+} cerebella, with and without irradiation at P1 (Two-way ANOVA, $F_{(1,34)}=6.768$, $p=0.0136$).

(D) Quantification of MitoTracker high expression at P2 in control and *mCAT*^{+/+} cerebella, with and without irradiation at P1 (Two-way ANOVA, $F_{(1,31)}=25.06$, $p<0.0001$).

(E) Quantification of TUNEL⁺ cell density in the EGL at P2 in control and *mCAT*^{+/+} cerebella, with and without irradiation at P1 (Two-way ANOVA, $F_{(1,14)}=87.56$, $p<0.0001$).

(F) Quantification of IBA1⁺ cell density in the EGL at P2 in control and *mCAT*^{+/+} cerebella, with and without irradiation at P1 (Two-way ANOVA, $F_{(1,14)}=15.58$, $p=0.0015$).

(G-J) Hematoxylin and eosin staining on mid-sagittal sections of P30 control and *mCAT*^{+/+} cerebellum with or without irradiation.

(K) Quantification of P30 cerebellar mid-sagittal section area in controls and *mCAT*^{+/+} nonIR and IR mice (Two-way ANOVA, $F_{(1,20)}=11.82$, $p=0.0026$).

(L) Graph showing the average area of mid-sagittal cerebellar sections at P3, P5, P8, P12 and P30 in control and *mCAT*^{+/+} non-irradiated and irradiated mice. Detailed statistics are shown in Supplementary Figure 4.

EGL, External granular layer; P, postnatal day; nonIR, non-irradiated; IR, irradiated. Scale bar: A and B: 100 μ m, F-I: 1mm. Significant *Tukey's post hoc* multiple comparison tests are shown in the figures and data are represented as mean \pm SEM.

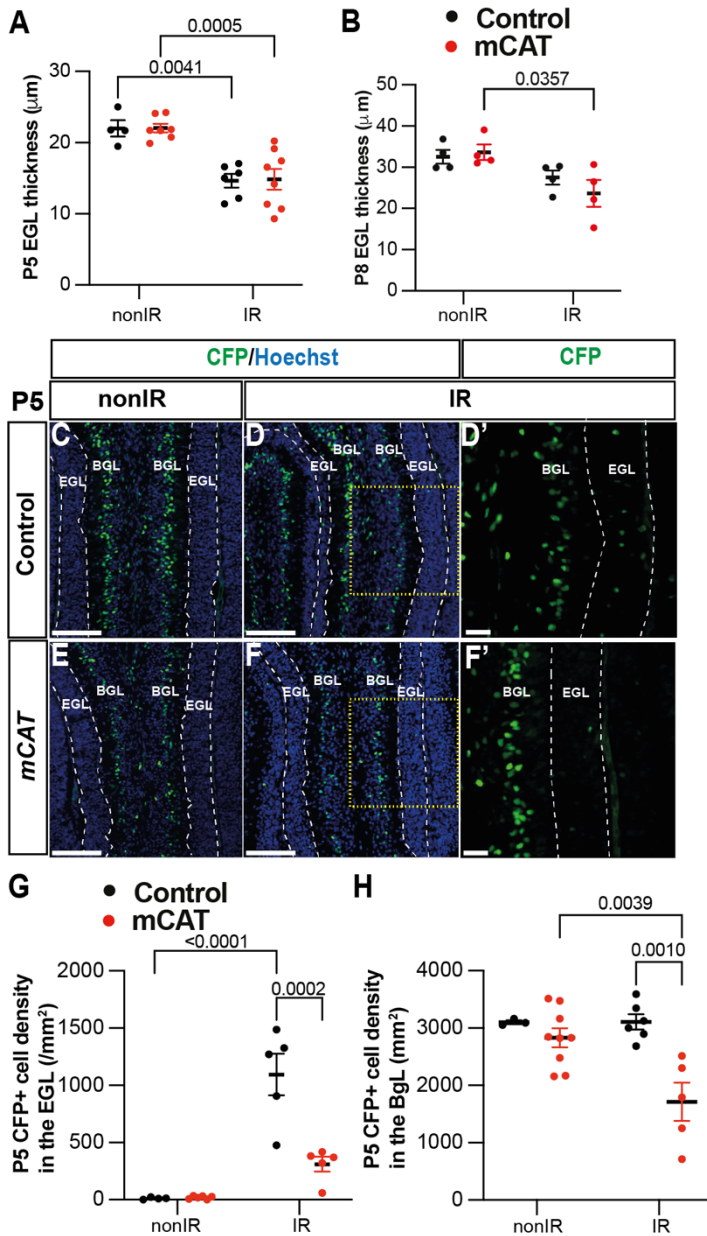


Figure 5: Reduced ROS impairs expansion of BgL-NEPs and their recruitment to the EGL after injury.

(A, B) Quantification of EGL thickness at P5 (Two-way ANOVA, $F_{(1,21)}=36.64$, $p<0.0001$) (A) and P8 (Two-way ANOVA, $F_{(1,12)}=11.34$, $p=0.0056$)(B) in lobules 3-5 of *Nes-Cfp/+* control and *Nes-Cfp/+; mCAT/+* mutant mice with and without irradiation at P1

(C-F) IHC staining of medial sagittal cerebellar sections showing expression of CFP (green) in the lobules 4/5 of *Nes-Cfp/+* control and *Nes-Cfp/+; mCAT/+* mutant mice at P5. Nuclei were counterstained with Hoechst (blue). (D') and (F') show a high-power images of the yellow boxed area in the single channel CFP. EGL is delineated by the dashed white lines.

(G, H) Quantification of CFP+ cell density in the EGL (Two-way ANOVA, $F_{(1,19)}=5.192$, $p=0.0359$) (G) and BgL (Two-way ANOVA, $F_{(1,17)}=6.191$, $p=0.0223$) (H) at P5 in *Nes-Cfp/+* control or *Nes-Cfp/+; mCAT/+* mutant non-irradiated and irradiated mice.

EGL, External granular layer; BgL, Bergmann glia Layer; P, postnatal day; nonIR, non-irradiated; IR, irradiated. Scale bar: D-F: 100 μm . Significant *Tukey's post hoc* multiple comparison tests are shown in the figures and data are represented as mean \pm SEM.

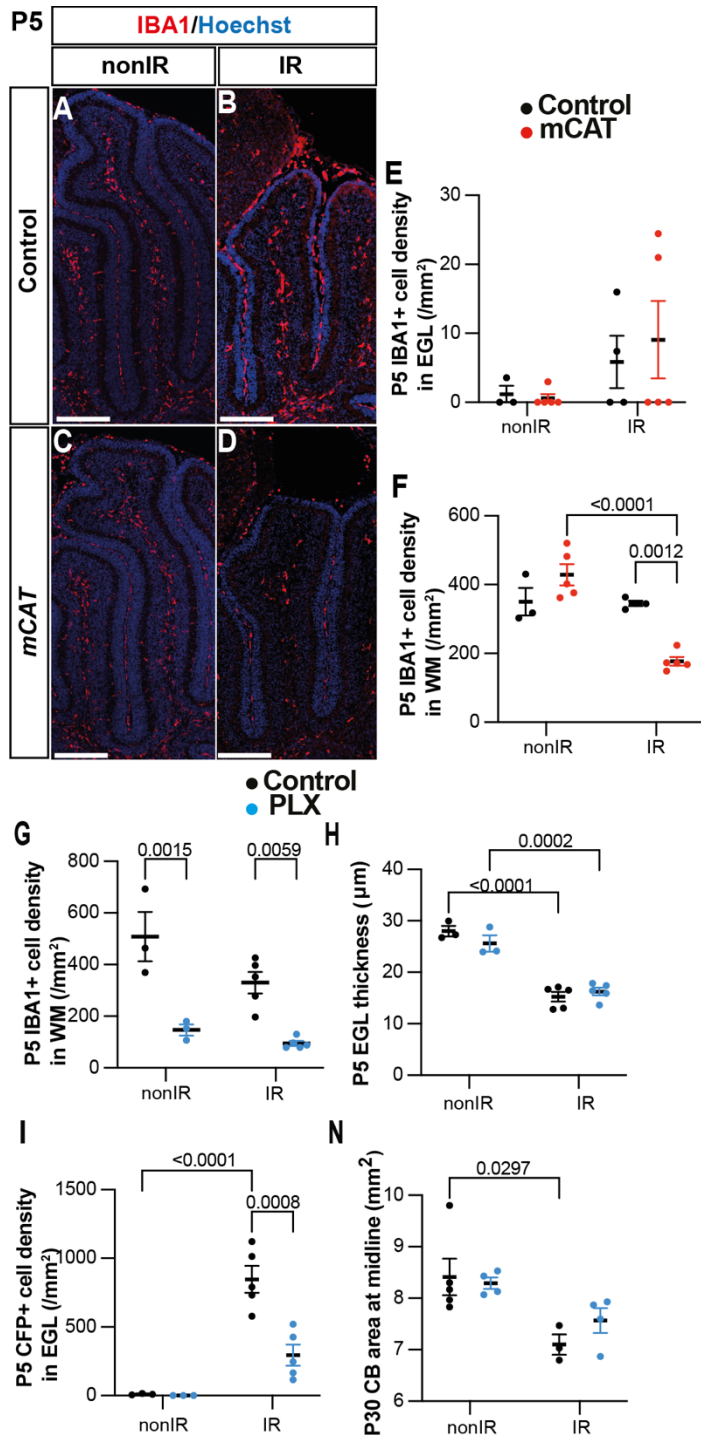


Figure 6: Microglia promote recruitment of NEPs to the EGL during cerebellar adaptive reprogramming after injury.

(A-D) IHC staining of medial sagittal cerebellar sections for IBA1 (red) in control and *mCAT*^{+/+} mice at P5. Nuclei were counterstained with Hoechst (blue).

(E, F) Quantification of IBA1+ cell density in the external granular layer (E) and white matter (Two-way ANOVA, $F_{(1,13)}=24.74$, $p=0.0003$) (F) at P5 on midsagittal sections of lobules 3-5 in the cerebellum of control and *mCAT*^{+/+} animals, with or without irradiation.

(G-J) IHC staining of medial sagittal cerebellar sections at P5 for CFP (green) in lobules 4/5 of *Nes-Cfp*^{+/+} mice treated with PLX5622 or control DMSO with or without irradiation. Nuclei were counterstained with Hoechst (blue). (H') and (J') show a high-power image of area indicated by yellow boxes. EGL is delineated by the white dashed lines.

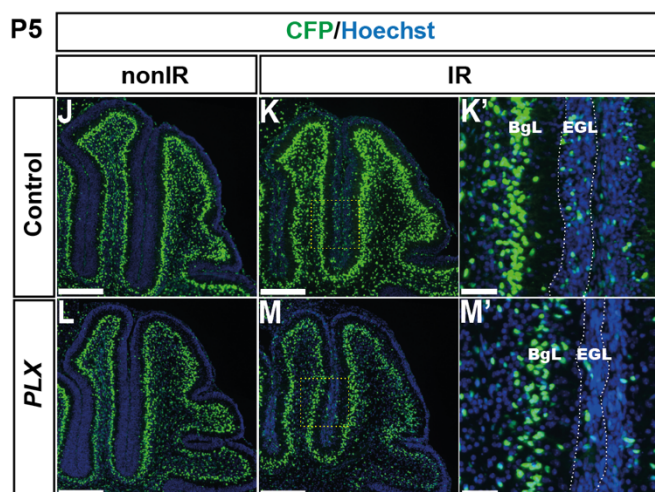
(K) Quantification of IBA1+ cell density in the white matter at P5 on mid-sagittal sections in lobules 3-5 of *Nes-Cfp*^{+/+} mice treated with PLX5622 or control DMSO, with or without irradiation (Two-way ANOVA, $F_{(1,12)}=42.40$, $p<0.001$).

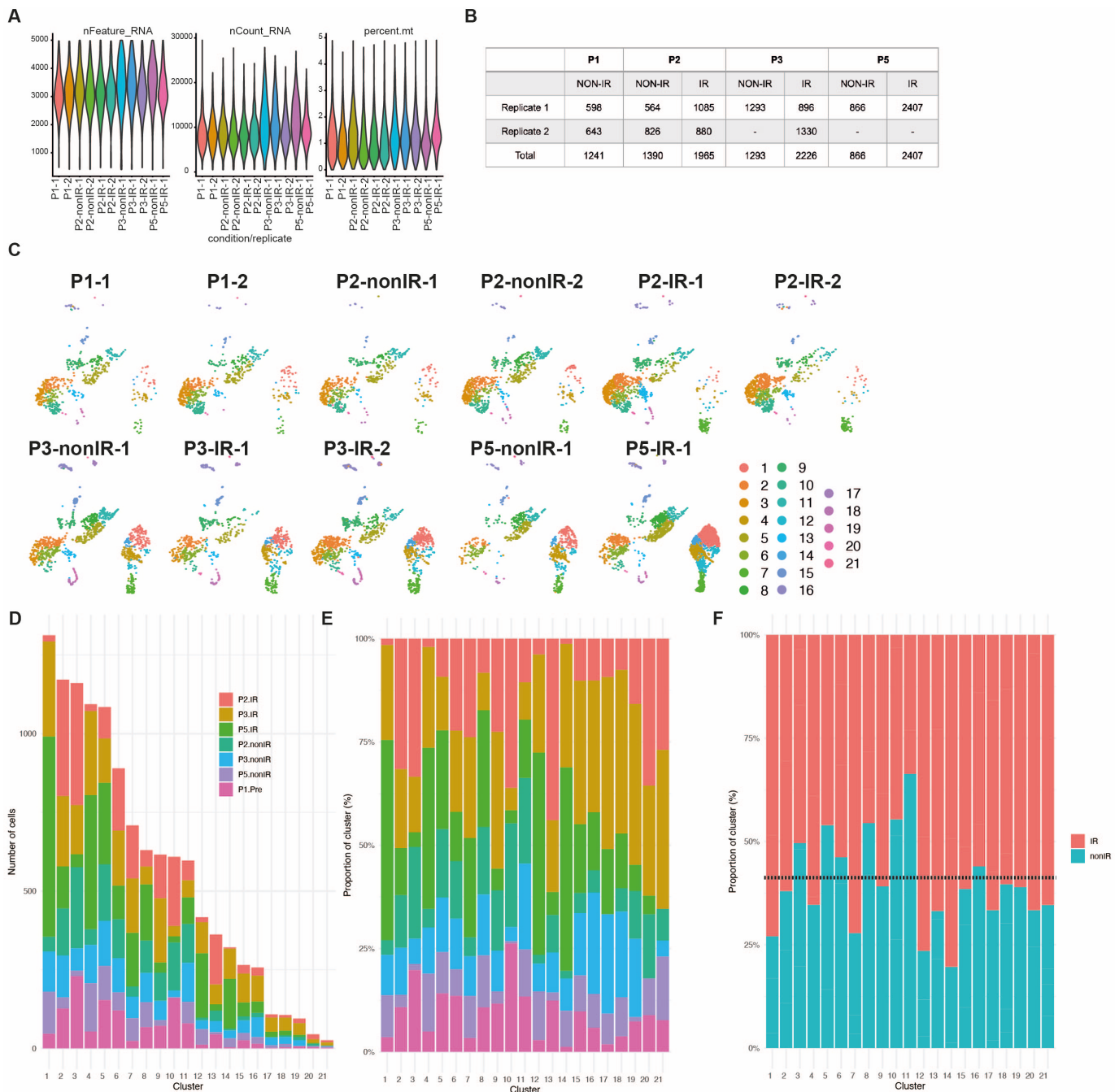
(L) Quantification of EGL thickness at P5 in lobules 3-5 of *Nes-Cfp*^{+/+} mice treated with PLX5622 or control DMSO with or without irradiation (Two-way ANOVA, $F_{(1,12)}=109.5$, $p<0.001$).

(M) Quantification of CFP+ cells density in the EGL at P5 on mid-sagittal sections in lobules 3-5 of *Nes-Cfp*^{+/+} mice treated with PLX5622 or control DMSO with or without irradiation (Two-way ANOVA, $F_{(1,12)}=10.62$, $p=0.0068$).

(N) Measurement of cerebellar mid-sagittal section area at P30 in controls or mice treated with PLX, with or without irradiation at P1 (Two-way ANOVA, $F_{(1,12)}=13.29$, $p=0.0034$).

EGL, External granular layer; WM, White matter; P, postnatal day; nonIR, non-irradiated; IR, irradiated. Scale bar: A-D and G-J: 250 μm. Significant *Tukey's post hoc* multiple comparison tests are shown in the figures and data are represented as mean ± SEM.





Supplementary Figure 1. scRNA-seq quality metrics and number of cells sequenced in each condition and biological replicate.

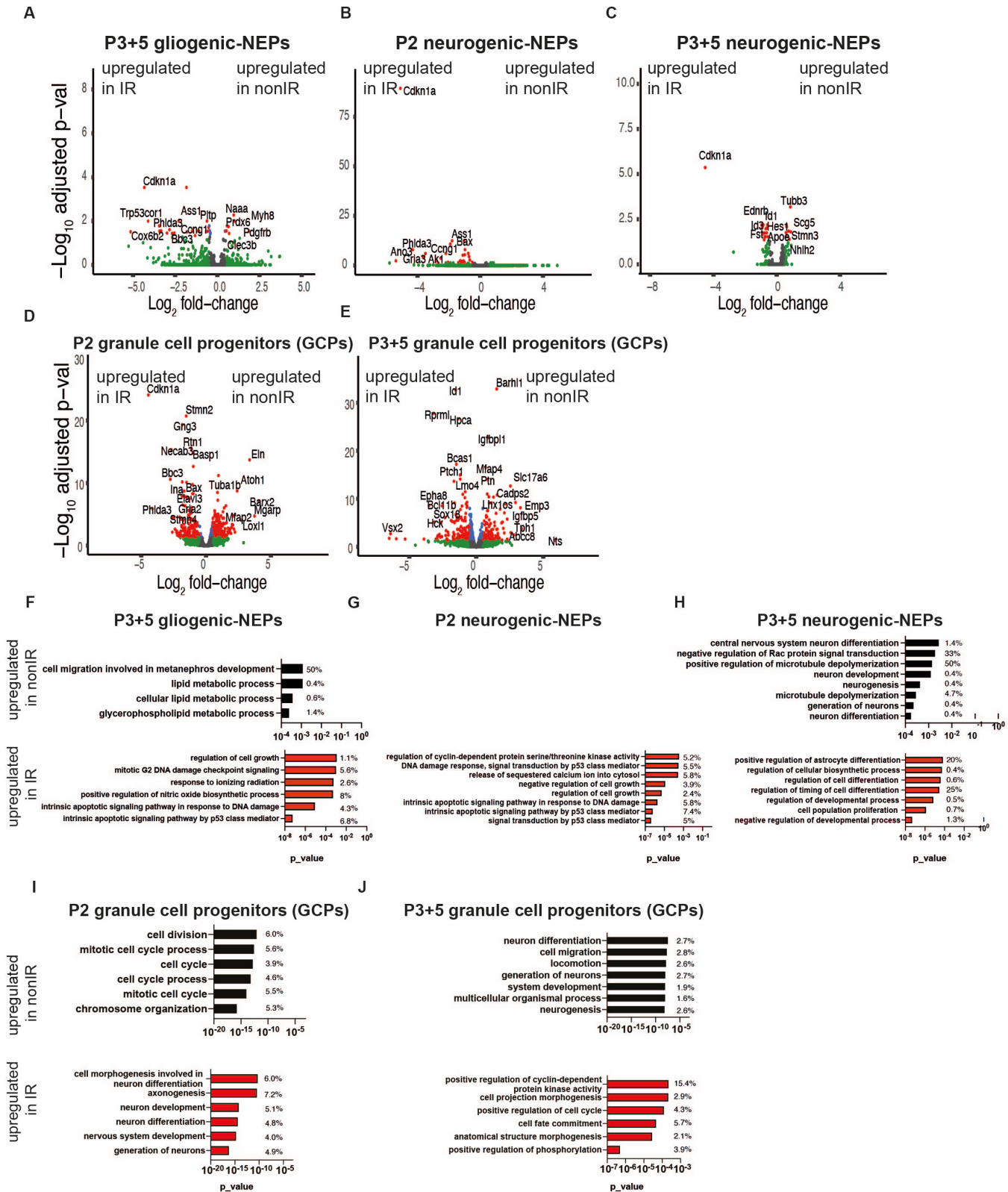
(A) Violin plots showing the number of features, RNA and percent mitochondrial RNA count across the biological replicates of the scRNA-seq data set after filtering the bad quality cells (cells were filtered out where number of detected genes was ≤ 1500 , the number of detected transcripts was $\geq 40,000$ and mitochondrial gene percentage $\geq 5\%$).

(B) Number of cells from each replicate and condition used for downstream analyses after filtering.

(C) UMAPs showing the distribution of cells across different clusters based on the samples.

(D-E) Number and proportion of cells from different ages and conditions in each cluster.

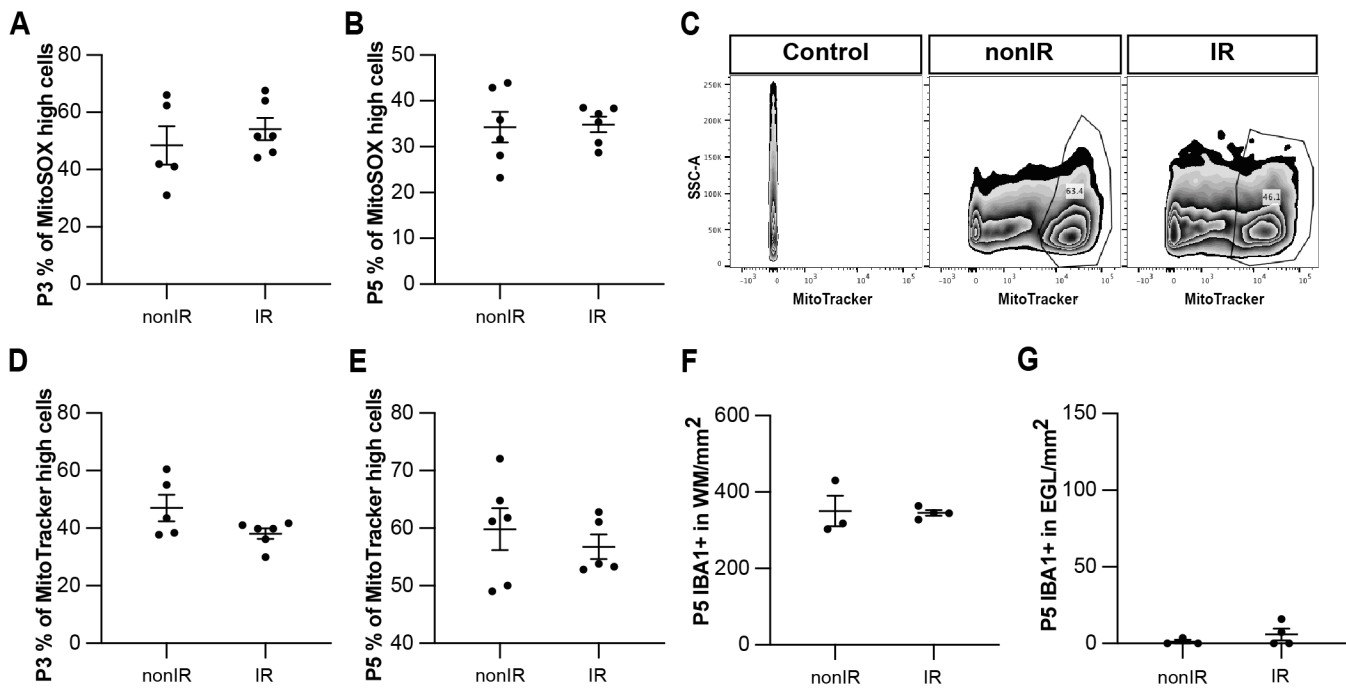
(F) Proportion of total nonIR (including P1) and IR cells in each cluster. Dotted line represents the expected ratio between the nonIR and IR cells.



Supplementary Figure 2: Injury induces distinct transcriptional changes in NEP subtypes and GCPs during adaptive reprogramming.

(A-E) Volcano plot showing differentially expressed genes in the P3+5 gliogenic-NEPs (A), P2 and P3+5 neurogenic NEPs (B, C) and P2 or P3+5 GCPs (D, E) (red: adjusted p -value ≤ 0.05 , \log_2 fold-change = 1, Table S2).

(F-J) Some of the significant GO terms associated with differentially expressed genes in the P3+5 gliogenic-NEPs (F), P2 or P3+5 neurogenic NEPs (G, H) and P2 or P3+5 GCPs (I, J) that were either upregulated in nonIR (top panel) or IR (bottom panel) (p -value ≤ 0.05).



Supplementary Figure 3: Irradiation of cerebella at P1 results in increased superoxide production and cell death and recruitment of microglia to the EGL that peaks at 24h.

(A, B) Quantification of high MitoSOX expression in nonIR and IR cerebella at P3 (A) and P5 (B).

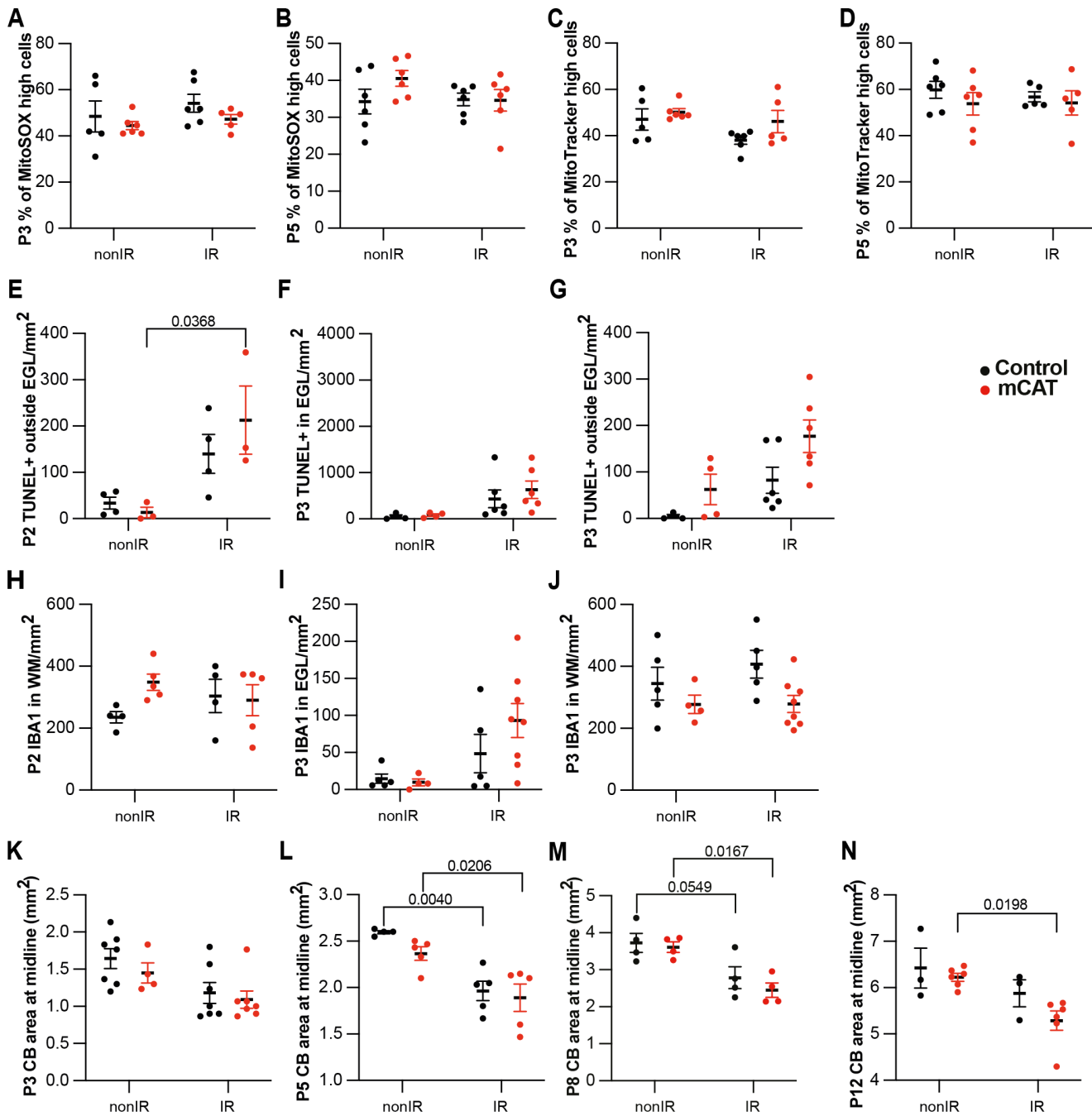
(C) Examples of flow cytometry analysis of mitochondria at P2 from nonIR and IR cerebella using MitoTracker dye. Gating determined the top 90% MitoTracker signal (MitoTracker high cells).

(D, E) Quantification of MitoTracker high expression in nonIR and IR cerebella at P3 (D) and P5 (E).

(F) Quantification of IBA1+ cell density in the WM at P5 in lobules 3-5 of nonIR and IR mice.

(G) Quantification of IBA1+ cell density in the EGL at P5 in lobules 3-5 of nonIR and IR mice.

EGL, External granular layer; WM, White matter; P, postnatal day; nonIR, non-irradiated; IR, irradiated. All statistical significance was determined using an unpaired t-test and data are represented as mean \pm SEM.



Supplementary Figure 4: Reduction of ROS impairs adaptive reprogramming and cerebellar repair.

(A, B) Quantification of high MitoSOX expression at P3 (A) and P5 (B) in control and *mCAT*^{+/+} cerebella, with and without irradiation at P1.

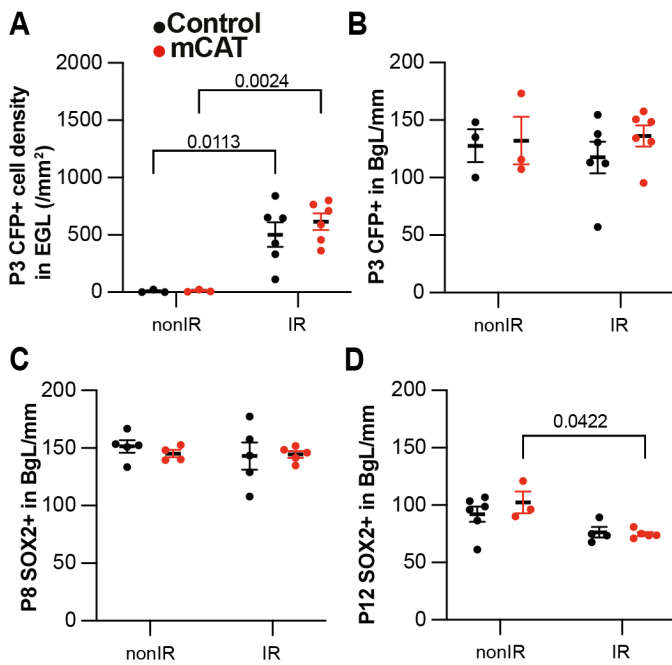
(C, D) Quantification of MitoTracker high expression at P3 (C) and P5 (D) in control and *mCAT*^{+/+} cerebella, with and without irradiation at P1.

(E-G) Quantification of TUNEL+ cell density outside EGL at P2 (Two-way ANOVA, $F_{(1,10)}=14.20$, $p=0.0037$) (E), at P3 (G), and in the EGL at P3 (F) in lobules 3-5 of nonIR and IR mice.

(H-J) Quantification of IBA1+ cell density in WM at P2 (H), at P3 (J), and in the EGL at P3 (I) in lobules 3-5 of nonIR and IR mice.

(K-N) Quantification of cerebellar midsagittal section area in controls and *mCAT*^{+/+} nonIR and IR mice at P3 (K), P5 (Two-way ANOVA, $F_{(1,15)}=28.52$, $p<0.001$) (L), P8 (Two-way ANOVA, $F_{(1,12)}=21.21$, $p=0.0006$) (M) and P12 (Two-way ANOVA, $F_{(1,14)}=9.682$, $p=0.0077$) (N).

EGL, External granular layer; WM, White matter; P, postnatal day; nonIR, non-irradiated; IR, irradiated. Significant *Tukey's post hoc* multiple comparison tests are shown in the figures and data are represented as mean \pm SEM.



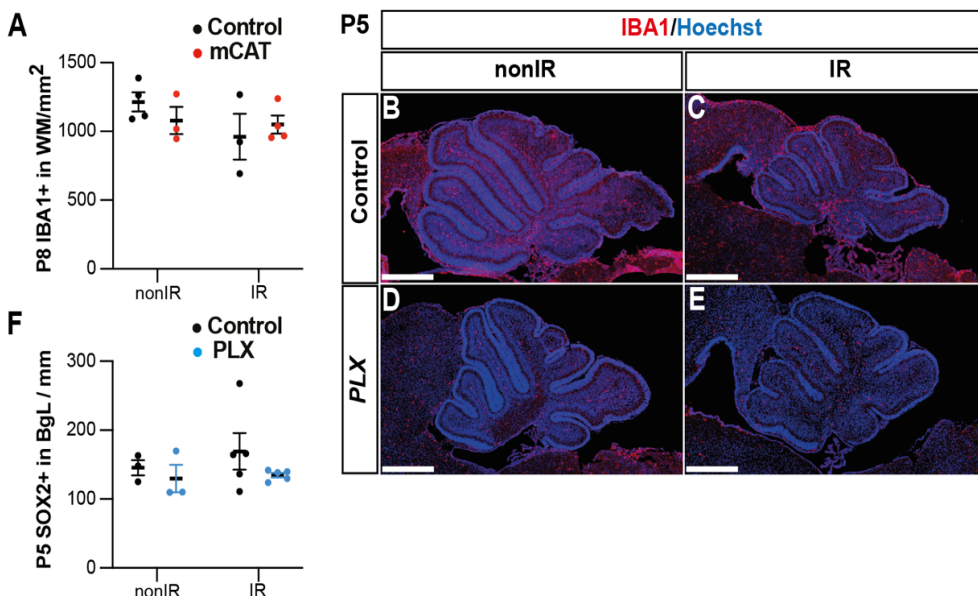
Supplementary Figure 5: Reduced ROS impairs expansion of BgL-NEPs and their migration to the EGL after injury.

(A) Quantification of CFP+ cell density in the EGL at P3 in *Nes-Cfp/+* control or *Nes-Cfp/+ mCAT* mutant nonIR and IR mice. (Two-way ANOVA, $F_{(1,14)}=33.77$, $p<0.0001$).

(B) Quantification of CFP+ cell normalized on BgL length at P5 in *Nes-Cfp/+* control or *Nes-Cfp/+ mCAT* mutant nonIR and IR mice.

(C, D) Quantification of SOX2+ NEP cell density on BgL length at P8 (C) and P12 (Two-way ANOVA, $F_{(1,12)}=12.50$, $p=0.0033$) (D) in control or *mCAT* mutant nonIR and IR mice.

EGL, External granular layer; BgL, Bergmann glia Layer; P, postnatal day; nonIR, non-irradiated; IR, irradiated. Significant *Tukey's post hoc* multiple comparison tests are shown in the figures and data are represented as mean \pm SEM.



Supplementary Figure 6: Microglia promote recruitment of NEPs to the EGL during cerebellar adaptive reprogramming after injury.

(A) Quantification of IBA1+ cell density in the WM at P8 in control or *mCAT* mutant nonIR and IR mice.

(B-E) Immunostaining of medial sagittal cerebellar sections at P5 showing expression of IBA1 (red) in mice treated with PLX5622 or control DMSO, with or without irradiation.

(F) Quantification of SOX2+ NEP cell density in the BgL at P5 in control or PLX treated nonIR and IR mice.

BgL, Bergmann glia Layer; WM, White Matter; P, postnatal day; nonIR, non-irradiated; IR, irradiated. Scale bar: 500 μm . Data are represented as mean \pm SEM.

Supplementary Tables

Antigen	Species	Concentration	References	Source
Catalase	Rabbit	1 to 100	01-05-030000	Athens Research & Technology
GFAP	Chicken	1 to 500	ab4674	Abcam
GFP	Rat	1 to 1000	440484	Nacalai Tesque
IBA1	Rabbit	1 to 500	019-19741	Wako Chemicals
SOX2	Goat	1 to 500	AF2018	R&D System

Table S1: List of antibodies and related information.

Table S2. Marker genes expressed by cluster in scRNA-seq dataset (irradiated at P1 (IR; P2, P3, P5) or non-irradiated (nonIR; P1, P2, P3, P5). pct1: % cells in a cluster that express the gene; pct2: % cells that express the gene outside the given cluster.

Table S3. Pseudobulk differential expression analysis between nonIR and IR gliogenic-NEPs (*Hopx*⁺, clusters 2, 3, 6, 10), neurogenic-NEPs (*Ascl1*⁺, clusters 5, 8, 11) and GCPs (*Atoh1*⁺, clusters 1,4,7,12,14) at P2, or at P3 and P5 (P3+5).

Table S4. GO Term analyses of differentially expressed genes (Table S3) of nonIR and IR gliogenic-NEPs (*Hopx*⁺, clusters 2, 3, 6, 10), neurogenic-NEPs (*Ascl1*⁺, clusters 5, 8, 11) and GCPs (*Atoh1*⁺, clusters 1,4,7,12,14) at P2, or at P3 and P5 (P3+5).

Table S5. Differentially open peaks at P2 identified by bulk ATAC-seq from nonIR and IR NEPs.

Table S6. Motif analysis of regions with increased accessibility in IR NEPs compared to the nonIR at P2.

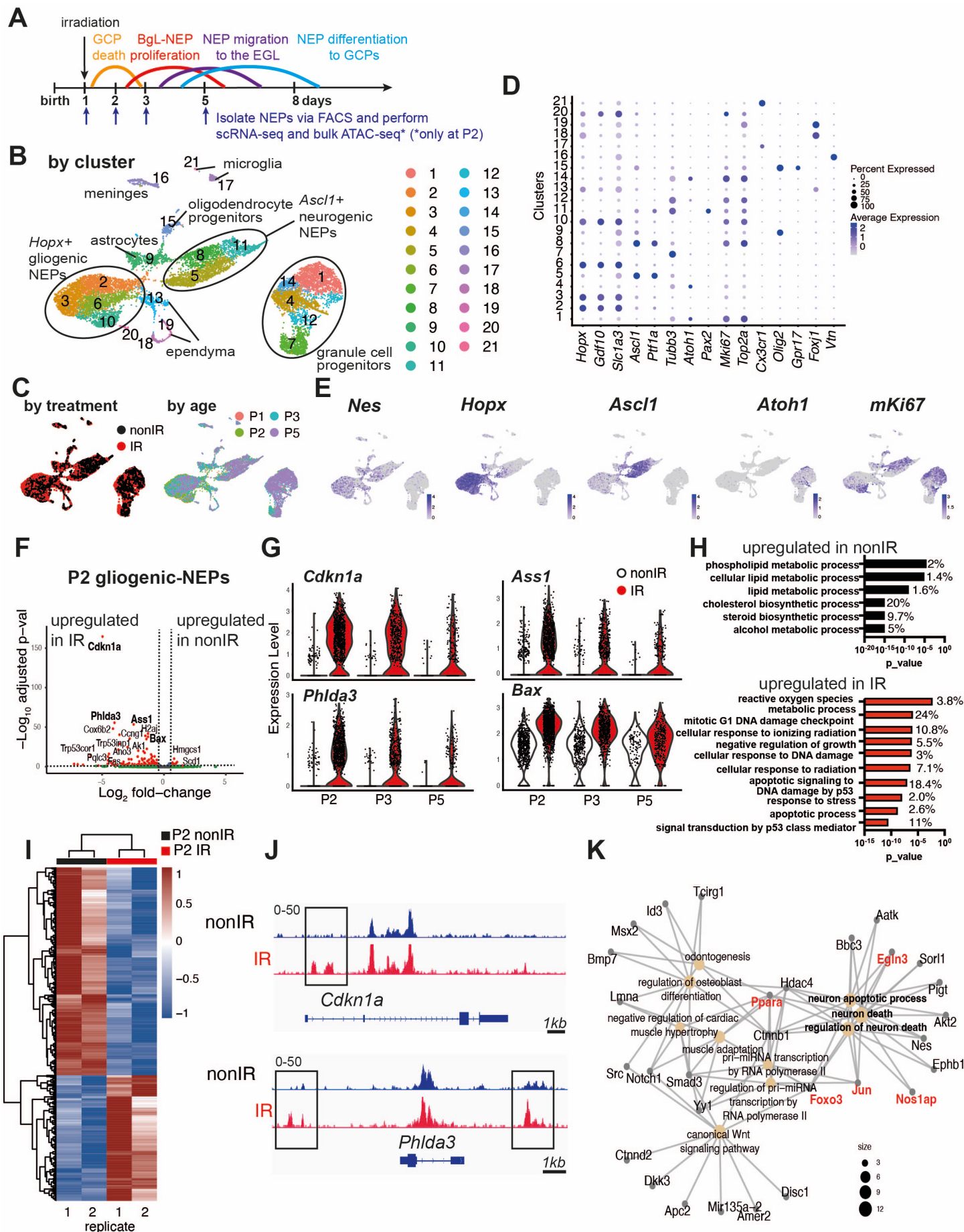


Figure 1: Injury induces ROS and cell stress signaling reflected by changes in the transcriptome and chromatin landscape of progenitors.

(A) Schematic summarizing the experimental plan.

(B-C) UMAP projections of 11,878 cells (6,978 nonIR and 4,900 IR) showing cluster annotations (B), treatment (black: nonIR, red: IR) and the age of the samples (red: P1, green: P2, blue: P3, purple: P5) (C).

(D) Dot plot showing the expression levels of key marker genes used for cluster annotation (gliogenic-NEPs: *Hopx*, *Gdf10*, *Slc1a3*, neurogenic-NEPs: *Ascl1*, *Ptf1a*, immature neurons: *Pax2*, GCPs: *Atoh1*, postmitotic neurons: *Tubb3*, microglia: *Cx3cr1*, oligodendrocyte progenitors: *Olig2*, oligodendrocytes: *Gpr17*, Ependymal cells: *Foxj1*).

(E) Feature plots showing *Nes*, *Hopx* (gliogenic-NEPs), *Ascl1* (neurogenic-NEPs) and *Atoh1* (GCPs) and *mKi67* (proliferation) expression highlighting the three main populations of interest. Clusters containing *Hopx*-NEPs (clusters 2, 3, 6, 10), *Ascl1*-NEPs (clusters 5, 8, 11), or GCPs (clusters 1, 4, 7, 12, 14) were subsetted from the original data set and were divided according to age (P2 or P3+P5) for the downstream differential expression analyses.

(F) Volcano plot showing differentially expressed genes in the P2 gliogenic-NEPs (red: adjusted p-value \leq 0.05, log₂fold-change $>$ |1|).

(G) Violin plots showing some of the top differentially expressed genes in P2 gliogenic-NEPs and how their expression changes over time with respect to their expression in control cells.

(H) Some of the significant GO terms associated with differentially expressed genes in P2 gliogenic-NEPs that were either upregulated in nonIR (top panel) or IR (bottom panel) cells (adjusted p-value \leq 0.05, Table S3).

(I) Heatmap showing differentially open chromatin regions in P2 nonIR and IR NEPs, identified by bulk ATAC-seq (1168 differentially open regions, adjusted p-value $<$ 0.05, Table S4).

(J) Tracks highlighting the injury-induced open chromatin regions around *Cdkn1a* and *Phlda3*, the top differentially expressed genes identified in (F).

(K) Linkages between genes and GO-terms identified by the ATAC-seq data revealed an active transcriptional network involved in regulating cell death and apoptosis. Genes colored in red (*Ppara*, *Egln3*, *Foxo3*, *Jun* and *Nos1ap*) have been implicated as upregulated with increased ROS levels or involved in ROS signaling.

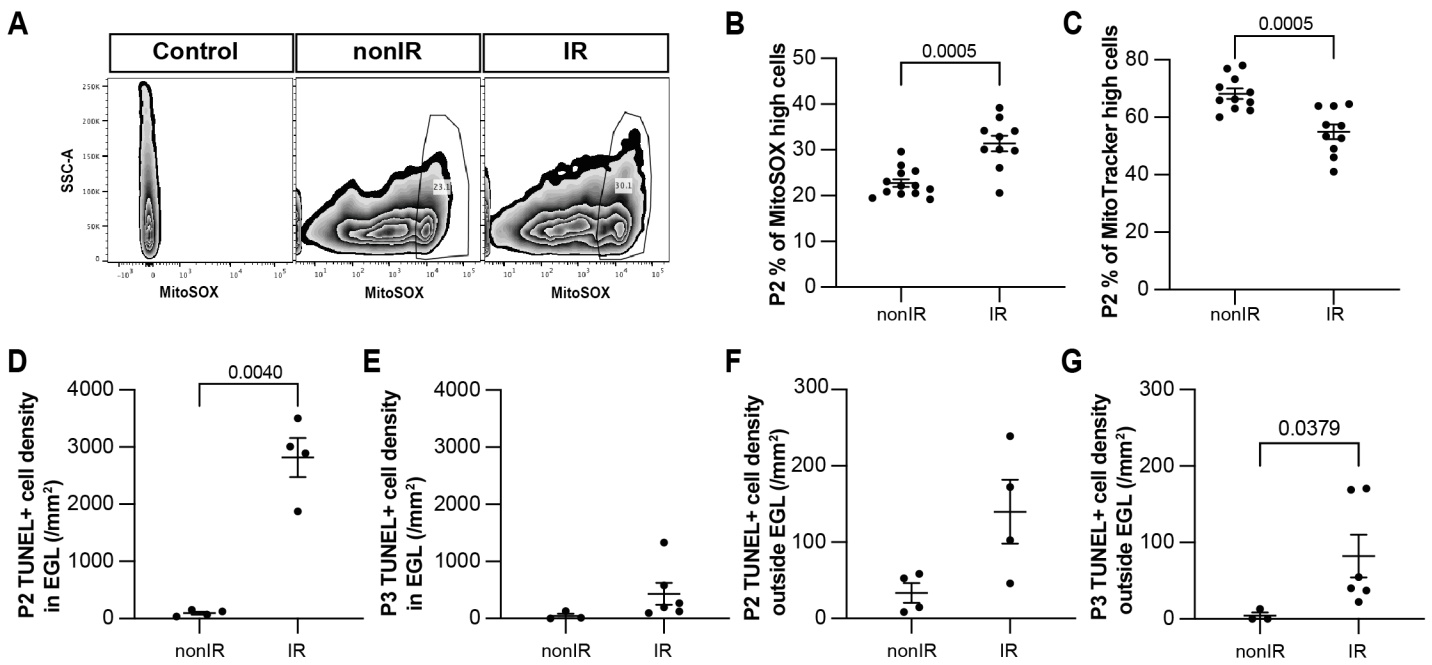


Figure 2: Cerebellar injury at P1 results in increased superoxide production, a reduction in mitochondria and increased cell death in the EGL that peaks 24h after injury.

(A) Examples of flow cytometry analysis of mitochondrial ROS at P2 from nonIR and IR cerebella using MitoSOX dye. Gating determined the top 90% MitoSOX signal (MitoSOX high cells).

(B, C) Quantification of MitoSOX high (B) and MitoTracker high (C) expression in nonIR and IR cerebella at P2.

(D, E) Quantification of TUNEL+ cell density in the EGL at P2 (D) and P3 (E) in lobules 3-5 of nonIR and IR mice.

(F, G) Quantification of TUNEL+ cell density outside the EGL at P2 (F) and P3 (G) in lobules 3-5 of nonIR and IR mice.

EGL, External granular layer; SSC, side scatter; P, postnatal day; nonIR, non-irradiated; IR, irradiated. All statistical significance was determined using an unpaired t-test and data are represented as mean \pm SEM.

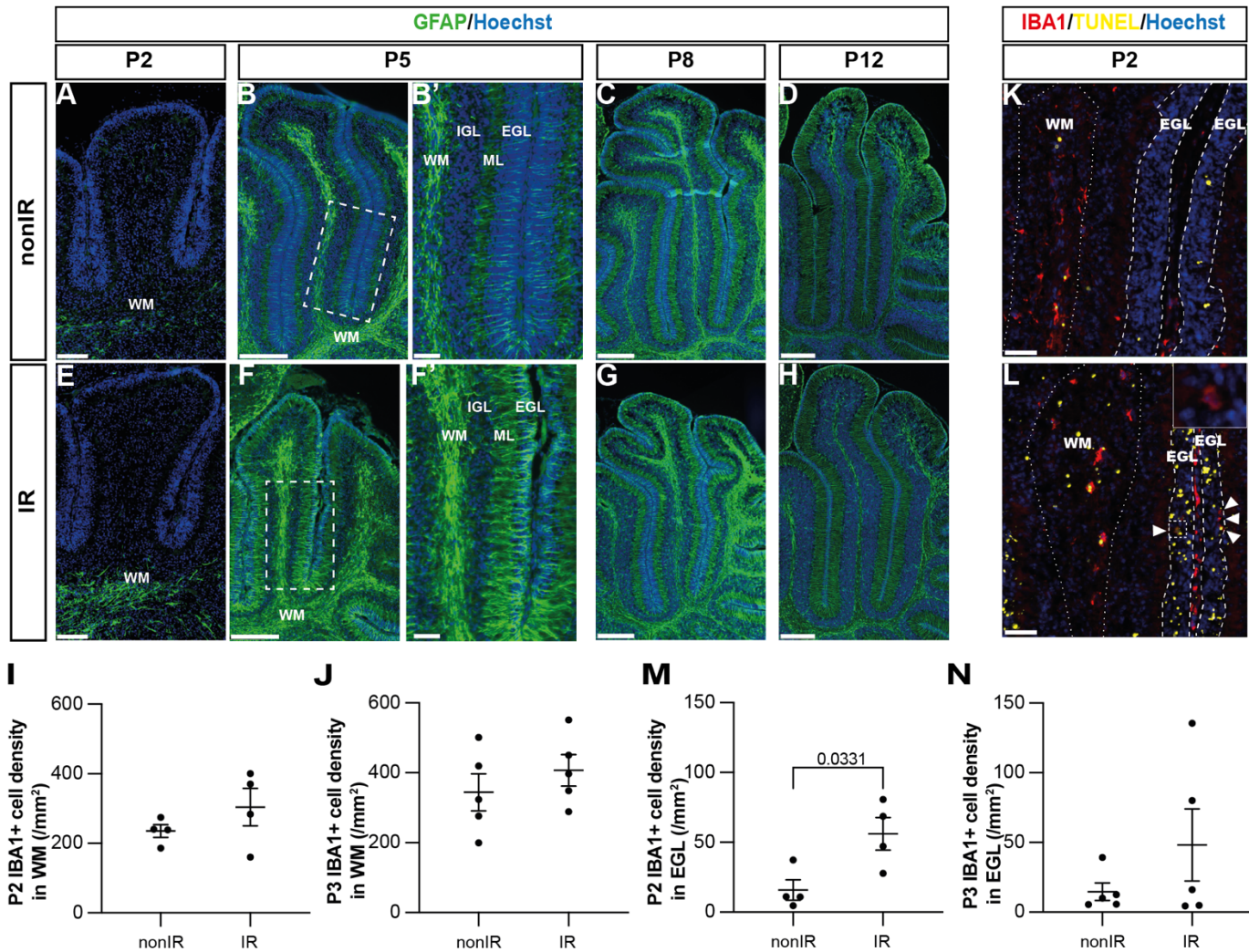


Figure 3: Cerebellar injury at P1 induces transient microglial recruitment to the EGL and prolonged astroglial microenvironment changes in the cerebellum.

(A-H) Immunohistochemical (IHC) staining of medial sagittal cerebellar sections for GFAP (green) in lobules 4/5 of nonIR and IR cerebellum at the stages indicated. Nuclei were counterstained with Hoechst. (B') and (F') show high-power images of white dashed line boxes in (B) and (F), respectively.

(I, J) Quantification of IBA1+ cell density in the WM at P2 (I) and P3 (J) in lobules 3-5 of nonIR and IR mice.

(K, L) IHC staining of medial sagittal cerebellar sections for IBA1 and TUNEL in lobule 3 of nonIR and IR cerebellum at P2. Nuclei were counterstained with Hoechst. White matter (WM) and external granular layer (EGL) are delineated by white dotted lines and dashed lines, respectively. High-power image in (L) of the area indicated by the white dashed line represents an IBA1+ cell present in the EGL. White arrowheads indicate additional IBA1+ cells in the EGL.

(M, N) Quantification of IBA1+ cell density in the EGL at P2 (M) and P3 (N) in lobules 3-5 of nonIR and IR mice.

EGL, External granular layer; WM, White matter; P, postnatal day; nonIR, non-irradiated; IR, irradiated. Scale bar: A and E 100 μm , B, C, D, E, F, G and H: 250 μm , B' and F': 50 μm , I and J: 50 μm . All statistical significance was determined using an unpaired t-test and data are represented as mean \pm SEM.

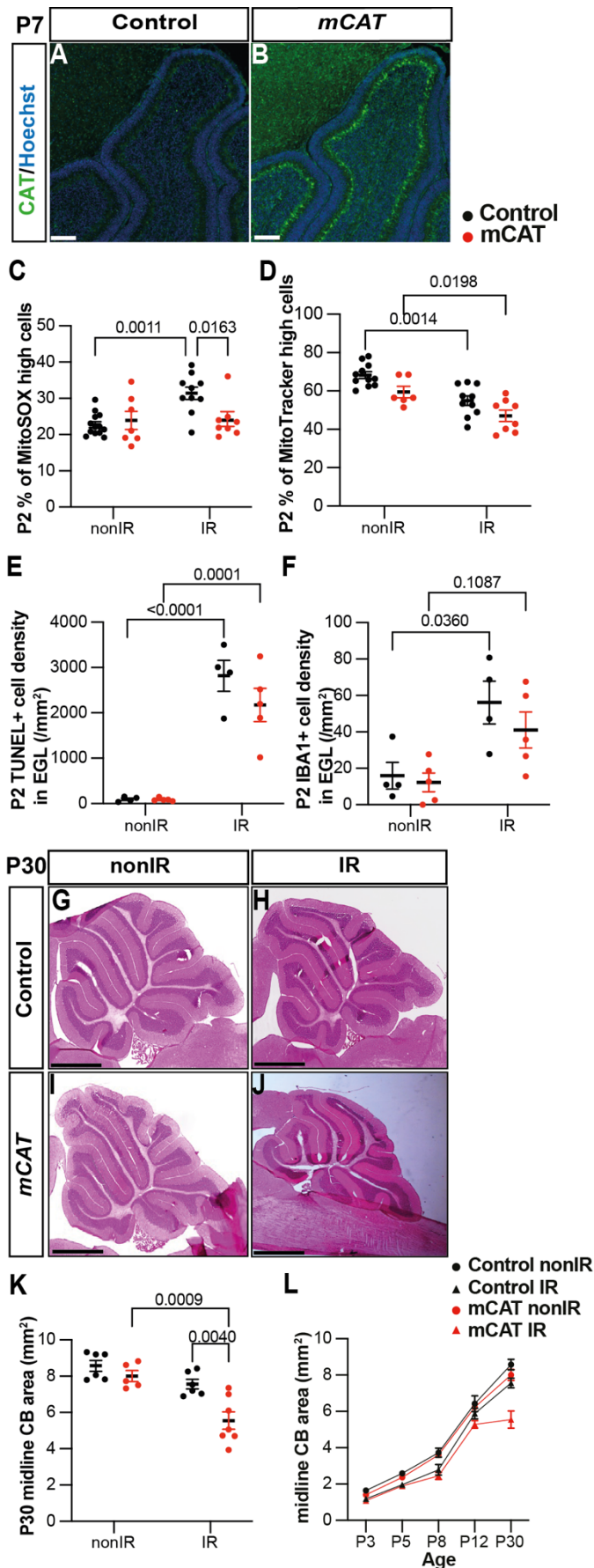


Figure 4: Reduction of ROS impairs adaptive reprogramming and cerebellar repair.

(A, B) IHC staining of medial sagittal cerebellar sections for human catalase in control (A) AND *mCAT*^{+/+} mice (B) at P7. Nuclei were counterstained with Hoechst (blue). Similar staining was seen in four *mCAT*^{+/+} mice.

(C) Quantification of MitoSOX high expression at P2 in control and *mCAT*^{+/+} cerebella, with and without irradiation at P1 (Two-way ANOVA, $F_{(1,34)}=6.768$, $p=0.0136$).

(D) Quantification of MitoTracker high expression at P2 in control and *mCAT*^{+/+} cerebella, with and without irradiation at P1 (Two-way ANOVA, $F_{(1,31)}=25.06$, $p<0.0001$).

(E) Quantification of TUNEL⁺ cell density in the EGL at P2 in control and *mCAT*^{+/+} cerebella, with and without irradiation at P1 (Two-way ANOVA, $F_{(1,14)}=87.56$, $p<0.0001$).

(F) Quantification of IBA1⁺ cell density in the EGL at P2 in control and *mCAT*^{+/+} cerebella, with and without irradiation at P1 (Two-way ANOVA, $F_{(1,14)}=15.58$, $p=0.0015$).

(G-J) Hematoxylin and eosin staining on mid-sagittal sections of P30 control and *mCAT*^{+/+} cerebellum with or without irradiation.

(K) Quantification of P30 cerebellar mid-sagittal section area in controls and *mCAT*^{+/+} nonIR and IR mice (Two-way ANOVA, $F_{(1,20)}=11.82$, $p=0.0026$).

(L) Graph showing the average area of mid-sagittal cerebellar sections at P3, P5, P8, P12 and P30 in control and *mCAT*^{+/+} non-irradiated and irradiated mice. Detailed statistics are shown in Supplementary Figure 4.

EGL, External granular layer; P, postnatal day; nonIR, non-irradiated; IR, irradiated. Scale bar: A and B: 100 μ m, F-I: 1mm. Significant *Tukey's post hoc* multiple comparison tests are shown in the figures and data are represented as mean \pm SEM.

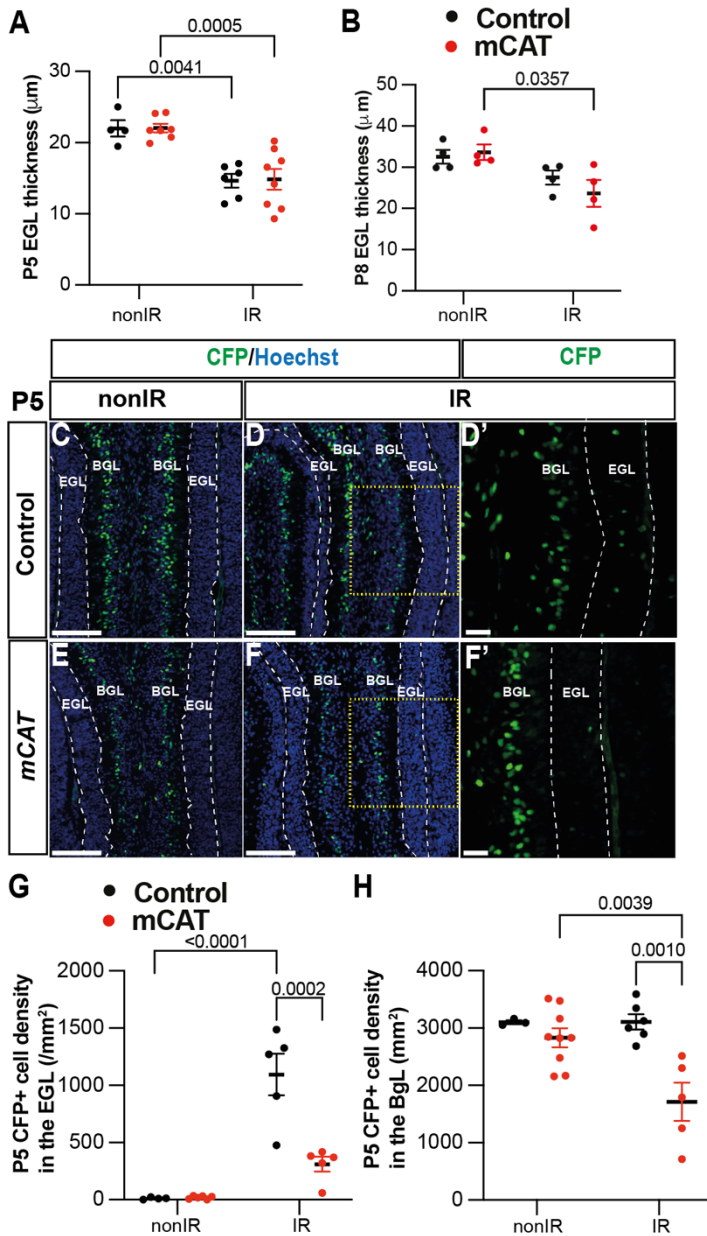


Figure 5: Reduced ROS impairs expansion of BgL-NEPs and their recruitment to the EGL after injury.

(A, B) Quantification of EGL thickness at P5 (Two-way ANOVA, $F_{(1,21)}=36.64$, $p<0.0001$) (A) and P8 (Two-way ANOVA, $F_{(1,12)}=11.34$, $p=0.0056$)(B) in lobules 3-5 of *Nes-Cfp/+* control and *Nes-Cfp/+; mCAT/+* mutant mice with and without irradiation at P1

(C-F) IHC staining of medial sagittal cerebellar sections showing expression of CFP (green) in the lobules 4/5 of *Nes-Cfp/+* control and *Nes-Cfp/+; mCAT/+* mutant mice at P5. Nuclei were counterstained with Hoechst (blue). (D') and (F') show a high-power images of the yellow boxed area in the single channel CFP. EGL is delineated by the dashed white lines.

(G, H) Quantification of CFP+ cell density in the EGL (Two-way ANOVA, $F_{(1,19)}=5.192$, $p=0.0359$) (G) and BgL (Two-way ANOVA, $F_{(1,17)}=6.191$, $p=0.0223$) (H) at P5 in *Nes-Cfp/+* control or *Nes-Cfp/+; mCAT/+* mutant non-irradiated and irradiated mice.

EGL, External granular layer; BgL, Bergmann glia Layer; P, postnatal day; nonIR, non-irradiated; IR, irradiated. Scale bar: D-F: 100 μm . Significant *Tukey's post hoc* multiple comparison tests are shown in the figures and data are represented as mean \pm SEM.

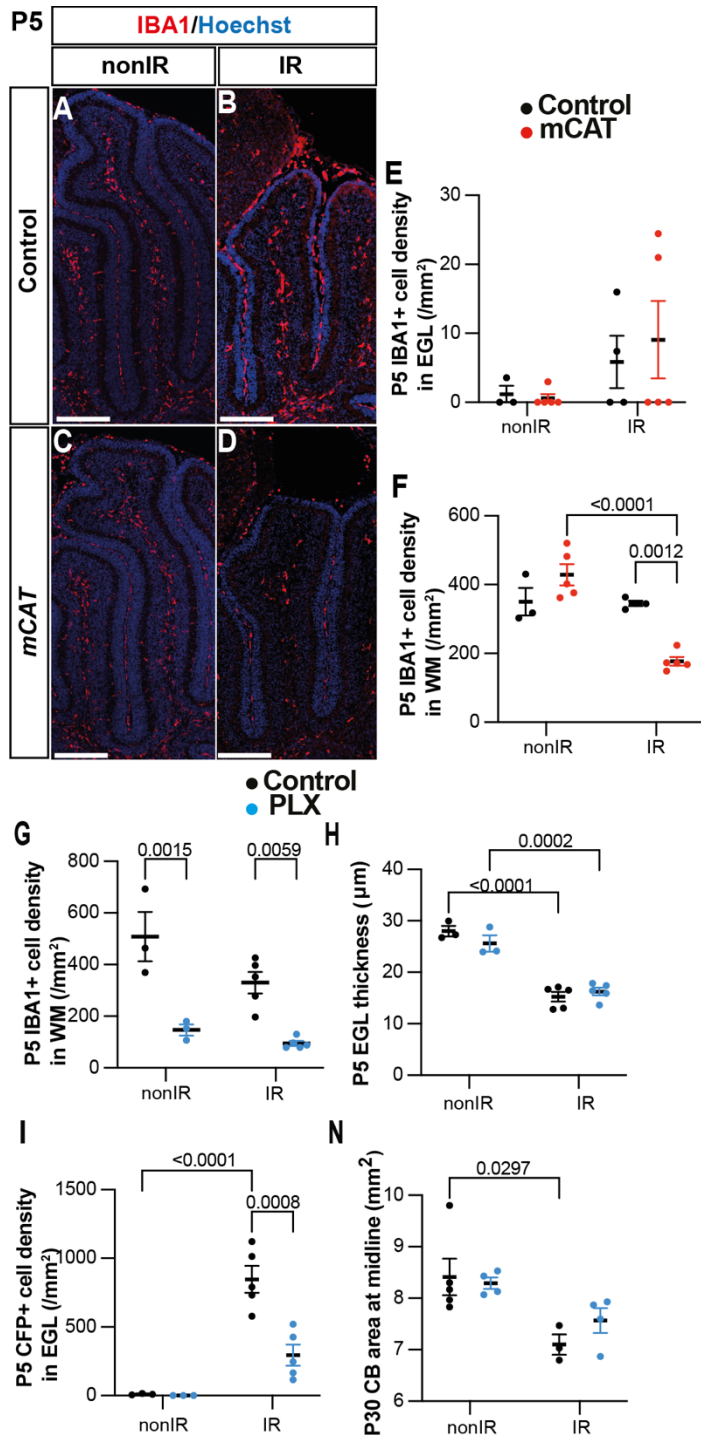


Figure 6: Microglia promote recruitment of NEPs to the EGL during cerebellar adaptive reprogramming after injury.

(A-D) IHC staining of medial sagittal cerebellar sections for IBA1 (red) in control and *mCAT*^{+/+} mice at P5. Nuclei were counterstained with Hoechst (blue).

(E, F) Quantification of IBA1⁺ cell density in the external granular layer (E) and white matter (Two-way ANOVA, $F_{(1,13)}=24.74$, $p=0.0003$) (F) at P5 on midsagittal sections of lobules 3-5 in the cerebellum of control and *mCAT*^{+/+} animals, with or without irradiation.

(G-J) IHC staining of medial sagittal cerebellar sections at P5 for CFP (green) in lobules 4/5 of *Nes-Cfp*^{+/+} mice treated with PLX5622 or control DMSO with or without irradiation. Nuclei were counterstained with Hoechst (blue). (H') and (J') show a high-power image of area indicated by yellow boxes. EGL is delineated by the white dashed lines.

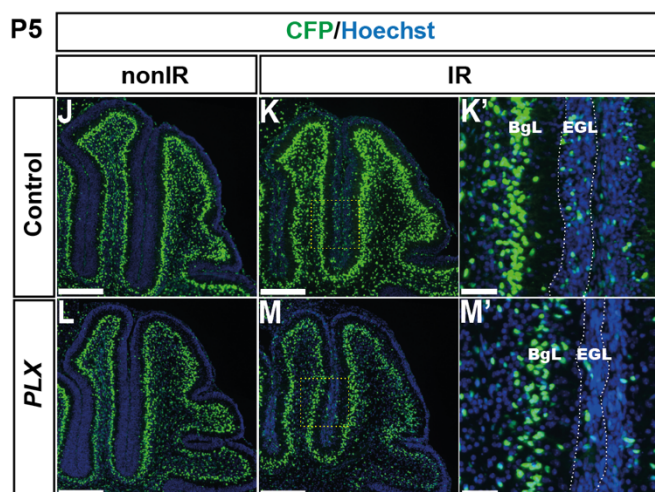
(K) Quantification of IBA1⁺ cell density in the white matter at P5 on mid-sagittal sections in lobules 3-5 of *Nes-Cfp*^{+/+} mice treated with PLX5622 or control DMSO, with or without irradiation (Two-way ANOVA, $F_{(1,12)}=42.40$, $p<0.001$).

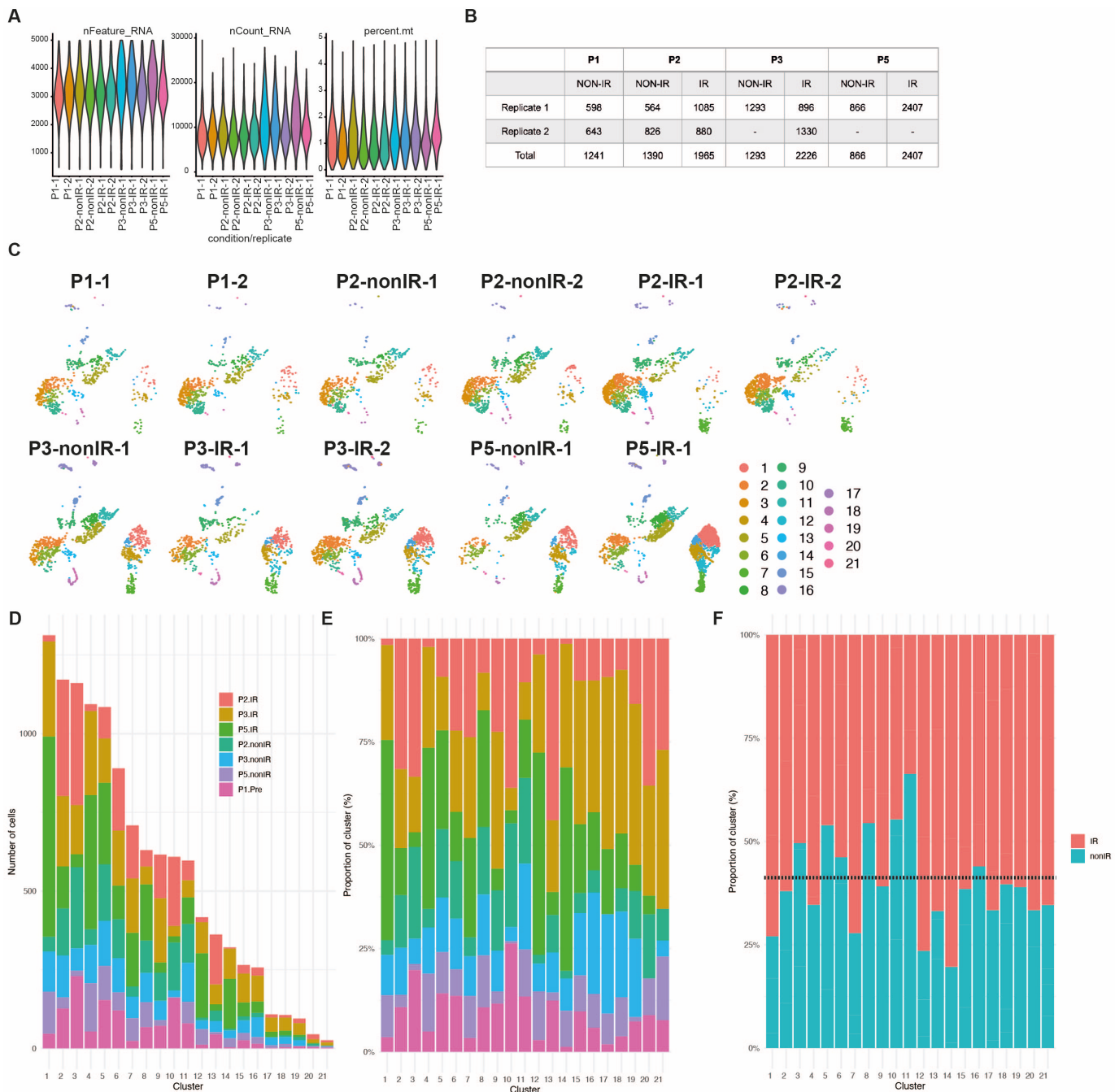
(L) Quantification of EGL thickness at P5 in lobules 3-5 of *Nes-Cfp*^{+/+} mice treated with PLX5622 or control DMSO with or without irradiation (Two-way ANOVA, $F_{(1,12)}=109.5$, $p<0.001$).

(M) Quantification of CFP⁺ cells density in the EGL at P5 on mid-sagittal sections in lobules 3-5 of *Nes-Cfp*^{+/+} mice treated with PLX5622 or control DMSO with or without irradiation (Two-way ANOVA, $F_{(1,12)}=10.62$, $p=0.0068$).

(N) Measurement of cerebellar mid-sagittal section area at P30 in controls or mice treated with PLX, with or without irradiation at P1 (Two-way ANOVA, $F_{(1,12)}=13.29$, $p=0.0034$).

EGL, External granular layer; WM, White matter; P, postnatal day; nonIR, non-irradiated; IR, irradiated. Scale bar: A-D and G-J: 250 µm. Significant *Tukey's post hoc* multiple comparison tests are shown in the figures and data are represented as mean ± SEM.





Supplementary Figure 1. scRNA-seq quality metrics and number of cells sequenced in each condition and biological replicate.

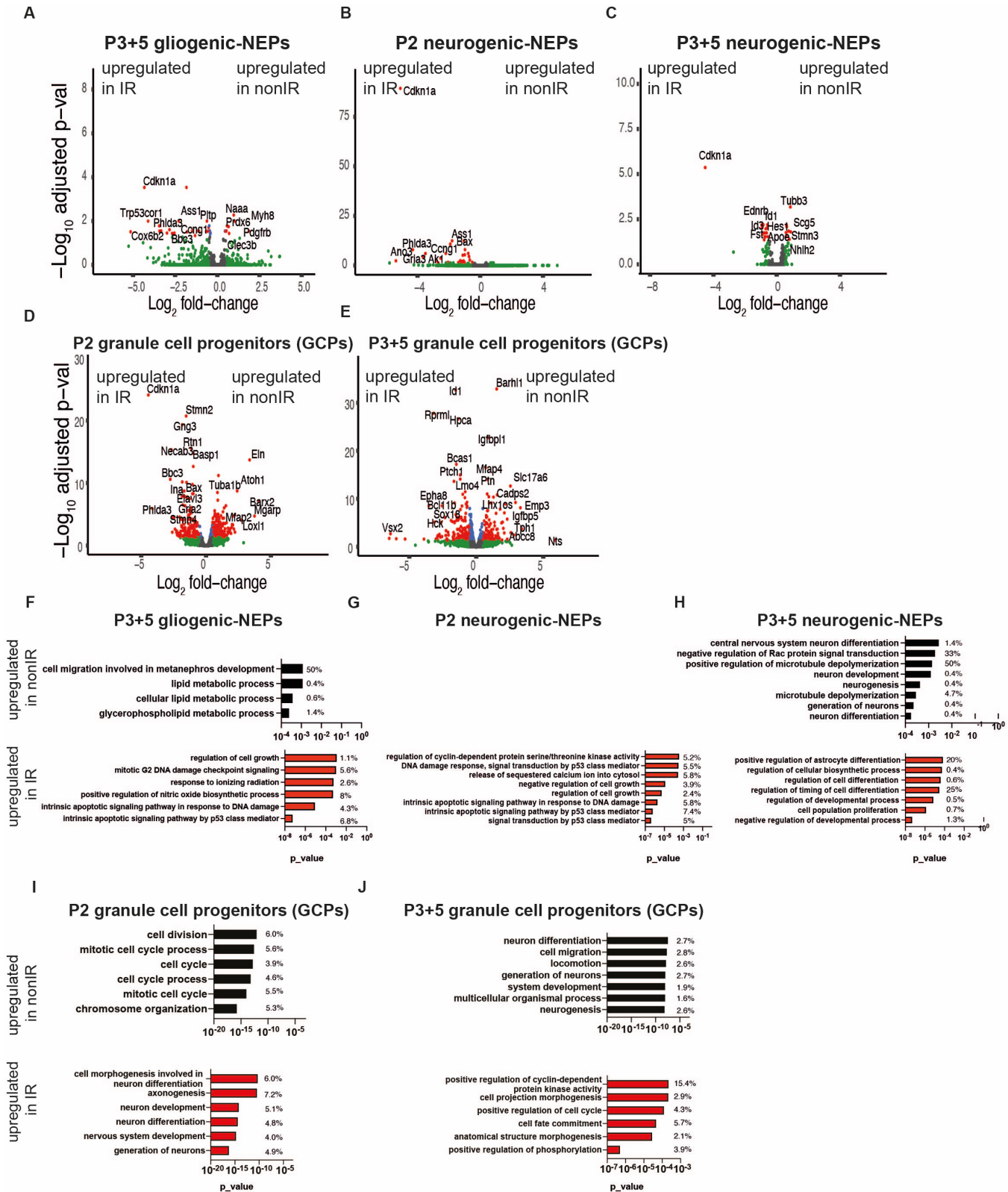
(A) Violin plots showing the number of features, RNA and percent mitochondrial RNA count across the biological replicates of the scRNA-seq data set after filtering the bad quality cells (cells were filtered out where number of detected genes was ≤ 1500 , the number of detected transcripts was $\geq 40,000$ and mitochondrial gene percentage $\geq 5\%$).

(B) Number of cells from each replicate and condition used for downstream analyses after filtering.

(C) UMAPs showing the distribution of cells across different clusters based on the samples.

(D-E) Number and proportion of cells from different ages and conditions in each cluster.

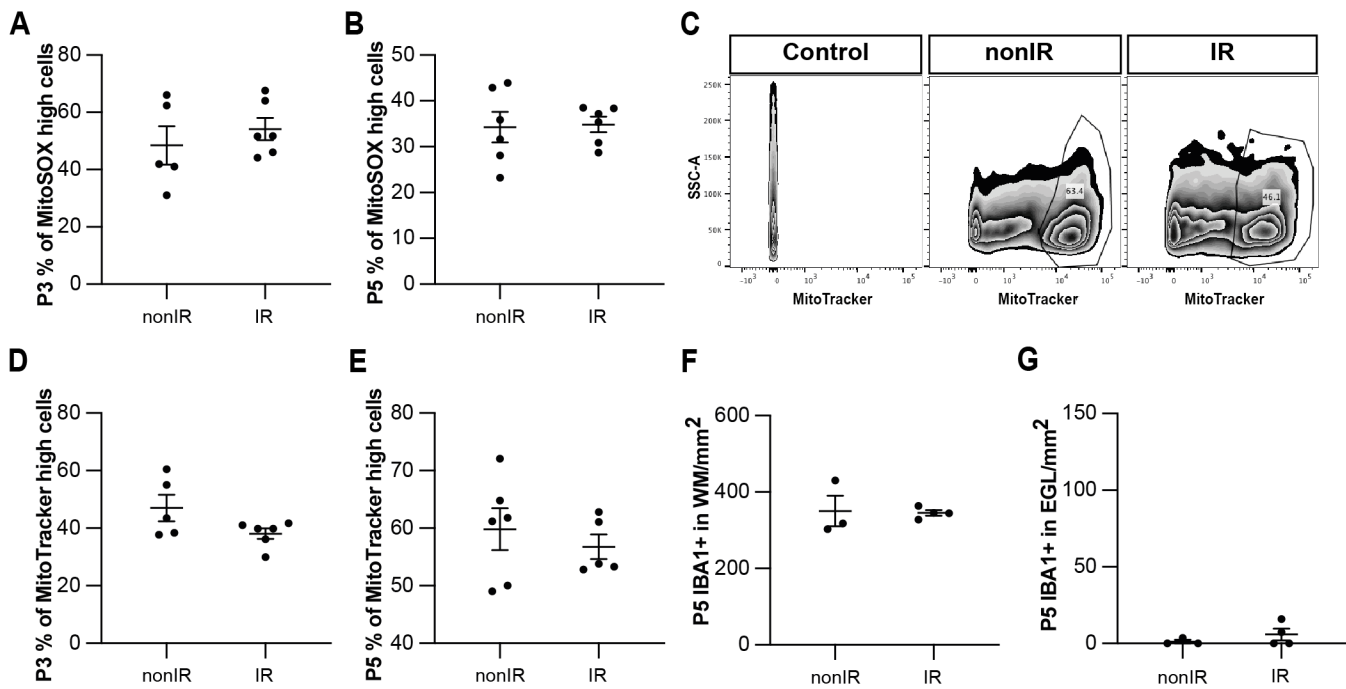
(F) Proportion of total nonIR (including P1) and IR cells in each cluster. Dotted line represents the expected ratio between the nonIR and IR cells.



Supplementary Figure 2: Injury induces distinct transcriptional changes in NEP subtypes and GCPs during adaptive reprogramming.

(A-E) Volcano plot showing differentially expressed genes in the P3+5 gliogenic-NEPs (A), P2 and P3+5 neurogenic NEPs (B, C) and P2 or P3+5 GCPs (D, E) (red: adjusted p-value \leq 0.05, log₂fold-change=1, Table S2).

(F-J) Some of the significant GO terms associated with differentially expressed genes in the P3+5 gliogenic-NEPs (F), P2 or P3+5 neurogenic NEPs (G, H) and P2 or P3+5 GCPs (I, J) that were either upregulated in nonIR (top panel) or IR (bottom panel) (p-value \leq 0.05).



Supplementary Figure 3: Irradiation of cerebella at P1 results in increased superoxide production and cell death and recruitment of microglia to the EGL that peaks at 24h.

(A, B) Quantification of high MitoSOX expression in nonIR and IR cerebella at P3 (A) and P5 (B).

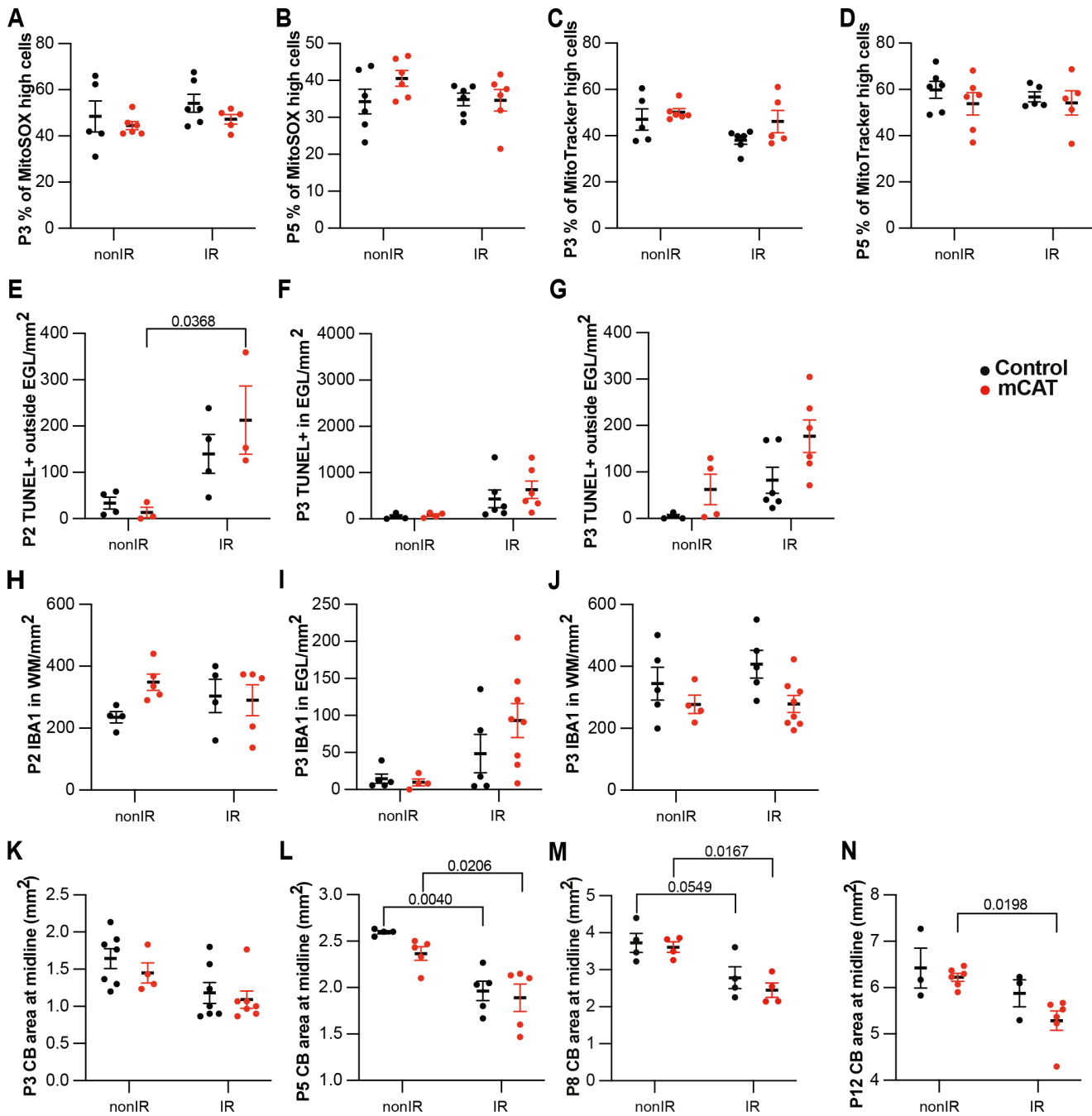
(C) Examples of flow cytometry analysis of mitochondria at P2 from nonIR and IR cerebella using MitoTracker dye. Gating determined the top 90% MitoTracker signal (MitoTracker high cells).

(D, E) Quantification of MitoTracker high expression in nonIR and IR cerebella at P3 (D) and P5 (E).

(F) Quantification of IBA1+ cell density in the WM at P5 in lobules 3-5 of nonIR and IR mice.

(G) Quantification of IBA1+ cell density in the EGL at P5 in lobules 3-5 of nonIR and IR mice.

EGL, External granular layer; WM, White matter; P, postnatal day; nonIR, non-irradiated; IR, irradiated. All statistical significance was determined using an unpaired t-test and data are represented as mean \pm SEM.



Supplementary Figure 4: Reduction of ROS impairs adaptive reprogramming and cerebellar repair.

(A, B) Quantification of high MitoSOX expression at P3 (A) and P5 (B) in control and *mCAT*^{+/+} cerebella, with and without irradiation at P1.

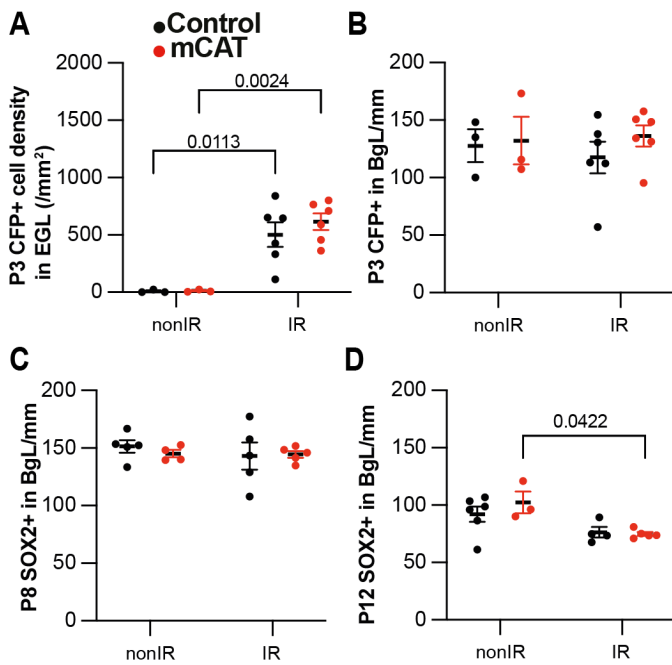
(C, D) Quantification of MitoTracker high expression at P3 (C) and P5 (D) in control and *mCAT*^{+/+} cerebella, with and without irradiation at P1.

(E-G) Quantification of TUNEL+ cell density outside EGL at P2 (Two-way ANOVA, $F_{(1,10)}=14.20$, $p=0.0037$) (E), at P3 (G), and in the EGL at P3 (F) in lobules 3-5 of nonIR and IR mice.

(H-J) Quantification of IBA1+ cell density in WM at P2 (H), at P3 (J), and in the EGL at P3 (I) in lobules 3-5 of nonIR and IR mice.

(K-N) Quantification of cerebellar midsagittal section area in controls and *mCAT*^{+/+} nonIR and IR mice at P3 (K), P5 (Two-way ANOVA, $F_{(1,15)}=28.52$, $p<0.001$) (L), P8 (Two-way ANOVA, $F_{(1,12)}=21.21$, $p=0.0006$) (M) and P12 (Two-way ANOVA, $F_{(1,14)}=9.682$, $p=0.0077$) (N).

EGL, External granular layer; WM, White matter; P, postnatal day; nonIR, non-irradiated; IR, irradiated. Significant *Tukey's post hoc* multiple comparison tests are shown in the figures and data are represented as mean \pm SEM.



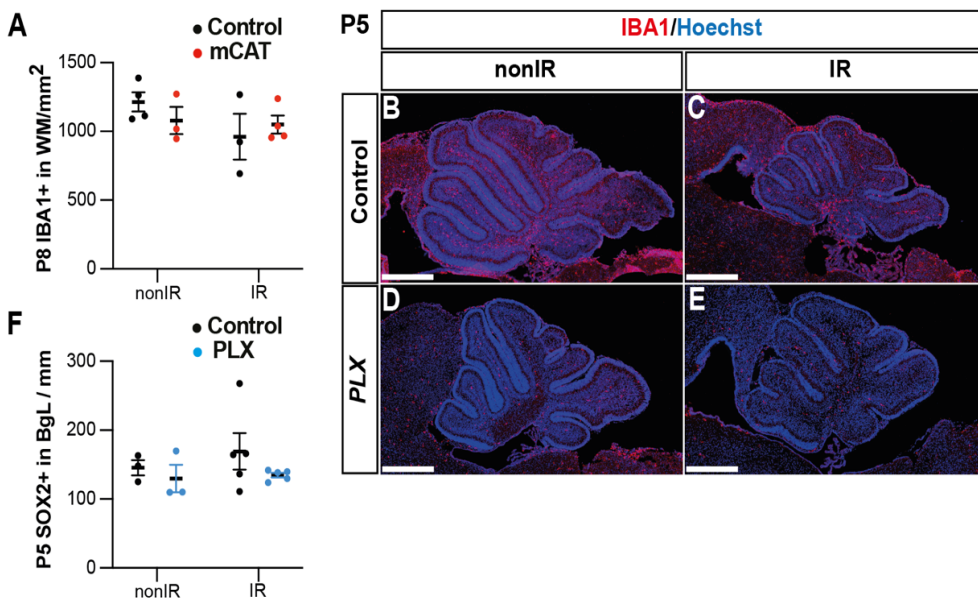
Supplementary Figure 5: Reduced ROS impairs expansion of BgL-NEPs and their migration to the EGL after injury.

(A) Quantification of CFP+ cell density in the EGL at P3 in *Nes-Cfp/+* control or *Nes-Cfp/+ mCAT* mutant nonIR and IR mice. (Two-way ANOVA, $F_{(1,14)}=33.77$, $p<0.0001$).

(B) Quantification of CFP+ cell normalized on BgL length at P5 in *Nes-Cfp/+* control or *Nes-Cfp/+ mCAT* mutant nonIR and IR mice.

(C, D) Quantification of SOX2+ NEP cell density on BgL length at P8 (C) and P12 (Two-way ANOVA, $F_{(1,12)}=12.50$, $p=0.0033$) (D) in control or *mCAT* mutant nonIR and IR mice.

EGL, External granular layer; BgL, Bergmann glia Layer; P, postnatal day; nonIR, non-irradiated; IR, irradiated. Significant *Tukey's post hoc* multiple comparison tests are shown in the figures and data are represented as mean \pm SEM.



Supplementary Figure 6: Microglia promote recruitment of NEPs to the EGL during cerebellar adaptive reprogramming after injury.

(A) Quantification of IBA1+ cell density in the WM at P8 in control or *mCAT* mutant nonIR and IR mice.

(B-E) Immunostaining of medial sagittal cerebellar sections at P5 showing expression of IBA1 (red) in mice treated with PLX5622 or control DMSO, with or without irradiation.

(F) Quantification of SOX2+ NEP cell density in the BgL at P5 in control or PLX treated nonIR and IR mice.

BgL, Bergmann glia Layer; WM, White Matter; P, postnatal day; nonIR, non-irradiated; IR, irradiated. Scale bar: 500 μm . Data are represented as mean \pm SEM.

Supplementary Tables

Antigen	Species	Concentration	References	Source
Catalase	Rabbit	1 to 100	01-05-030000	Athens Research & Technology
GFAP	Chicken	1 to 500	ab4674	Abcam
GFP	Rat	1 to 1000	440484	Nacalai Tesque
IBA1	Rabbit	1 to 500	019-19741	Wako Chemicals
SOX2	Goat	1 to 500	AF2018	R&D System

Table S1: List of antibodies and related information.

Table S2. Marker genes and all genes expressed by cluster in scRNA-seq dataset for irradiated at P1 (IR; P2, P3, P5) or non-irradiated (nonIR; P1, P2, P3, P5). pct1: % cells in a cluster that express the gene; pct2: % cells that express the gene outside the given cluster.

Table S3. Pseudobulk differential expression analysis between nonIR and IR gliogenic-NEPs (*Hopx*⁺, clusters 2, 3, 6, 10), neurogenic-NEPs (*Ascl1*⁺, clusters 5, 8, 11) and GCPs (*Atoh1*⁺, clusters 1,4,7,12,14) at P2, or at P3 and P5 (P3+5).

Table S4. GO Term analyses of differentially expressed genes (Table S3) of nonIR and IR gliogenic-NEPs (*Hopx*⁺, clusters 2, 3, 6, 10), neurogenic-NEPs (*Ascl1*⁺, clusters 5, 8, 11) and GCPs (*Atoh1*⁺, clusters 1,4,7,12,14) at P2, or at P3 and P5 (P3+5).

Table S5. Differentially open peaks at P2 identified by bulk ATAC-seq from nonIR and IR NEPs.

Table S6. Motif analysis of regions with increased accessibility in IR NEPs compared to the nonIR at P2.